


## Article

# ELULC-10, a 10 m European Land Use and Land Cover Map Using Sentinel and Landsat Data in Google Earth Engine

S. Mohammad Mirmazloumi <sup>1,\*</sup> , Mohammad Kakooei <sup>2</sup> , Farzane Mohseni <sup>3,4</sup> , Arsalan Ghorbanian <sup>3,4</sup> , Meisam Amani <sup>5</sup> , Michele Crosetto <sup>1</sup> and Oriol Monserrat <sup>1</sup> 

- <sup>1</sup> Geomatics Research Unit, Centre Tecnològic de Telecomunicacions de Catalunya (CTTC/CERCA), Av. Gauss 7, 08860 Castelldefels, Barcelona, Spain; michele.crosetto@cttc.cat (M.C.); oriol.monserrat@cttc.cat (O.M.)
  - <sup>2</sup> Department of Computer Science, Chalmers University of Technology, Rännvägen 6, 412 58 Göteborg, Sweden; kakooei@chalmers.se
  - <sup>3</sup> Department of Photogrammetry and Remote Sensing, Faculty of Geodesy and Geomatics Engineering, K. N. Toosi University of Technology, Tehran 19967 15433, Iran; farzanemohseni@email.kntu.ac.ir (F.M.); a.ghorbanian@email.kntu.ac.ir (A.G.)
  - <sup>4</sup> Department of Technology and Society, Faculty of Engineering, Lund University, 221 00 Lund, Sweden
  - <sup>5</sup> Wood Environment & Infrastructure Solutions, Ottawa, ON CA K2E 7L5, Canada; meisam.amani@woodplc.com
- \* Correspondence: sm.mirmazloumi@cttc.es

**Abstract:** Land Use/Land Cover (LULC) maps can be effectively produced by cost-effective and frequent satellite observations. Powerful cloud computing platforms are emerging as a growing trend in the high utilization of freely accessible remotely sensed data for LULC mapping over large-scale regions using big geodata. This study proposes a workflow to generate a 10 m LULC map of Europe with nine classes, ELULC-10, using European Sentinel-1/-2 and Landsat-8 images, as well as the LUCAS reference samples. More than 200 K and 300 K of in situ surveys and images, respectively, were employed as inputs in the Google Earth Engine (GEE) cloud computing platform to perform classification by an object-based segmentation algorithm and an Artificial Neural Network (ANN). A novel ANN-based data preparation was also presented to remove noisy reference samples from the LUCAS dataset. Additionally, the map was improved using several rule-based post-processing steps. The overall accuracy and kappa coefficient of 2021 ELULC-10 were 95.38% and 0.94, respectively. A detailed report of the classification accuracies was also provided, demonstrating an accurate classification of different classes, such as Woodland and Cropland. Furthermore, rule-based post processing improved LULC class identifications when compared with current studies. The workflow could also supply seasonal, yearly, and change maps considering the proposed integration of complex machine learning algorithms and large satellite and survey data.

**Keywords:** remote sensing; LULC; Europe; Google Earth Engine; LUCAS; Sentinel; Landsat-8



**Citation:** Mirmazloumi, S.M.; Kakooei, M.; Mohseni, F.; Ghorbanian, A.; Amani, M.; Crosetto, M.; Monserrat, O. ELULC-10, a 10 m European Land Use and Land Cover Map Using Sentinel and Landsat Data in Google Earth Engine. *Remote Sens.* **2022**, *14*, 3041. <https://doi.org/10.3390/rs14133041>

Academic Editor: Georgios Mallinis

Received: 1 June 2022

Accepted: 22 June 2022

Published: 24 June 2022

**Publisher's Note:** MDPI stays neutral with regard to jurisdictional claims in published maps and institutional affiliations.



**Copyright:** © 2022 by the authors. Licensee MDPI, Basel, Switzerland. This article is an open access article distributed under the terms and conditions of the Creative Commons Attribution (CC BY) license (<https://creativecommons.org/licenses/by/4.0/>).

## 1. Introduction

Land Use/Land Cover (LULC) maps provide valuable information for defining the terrestrial and atmospheric interactions of the Earth and providing a realistic picture of human activities and natural environment interconnections. Policymakers require accurate geoinformation about the interactions between human activities and the environment, to maintain and improve sustainable development and planning strategies. In this regard, Remote Sensing (RS) systems acquire valuable datasets, which can be efficiently applied to various applications, such as urban planning [1–3], water management [4,5], nature conservation [6–8], natural resource monitoring [9–11], habitat distribution assessment [12–14], and LULC mapping [15,16].

Satellite imagery, along with advanced Machine Learning (ML) algorithms and cloud computing platforms, has significantly facilitated accurate large-scale LULC mapping [17–20].

Due to the availability of various types of Earth Observation (EO) data, numerous LULC products in the range from 10 m to 1 km spatial resolutions have been generated over different parts of the world. To this end, various satellite datasets, such as the Copernicus Programme (Sentinel) [19–26], Earth Resources Technology Satellite of National Aeronautics and Space Administration (NASA)/United States Geological Survey (USGS) program (Landsat) [27–30], AVHRR instrument of National Oceanic and Atmospheric Administration [31–33], and the Moderate Resolution Imaging Spectroradiometer of NASA (MODIS) [34–36] have been employed. It is worth noting that although RS has many advantages for LULC classification, in situ data plays a significant role in obtaining high classification accuracy from supervised classification methods.

Powerful cloud computing platforms are required when the objective is large-scale LULC mapping of analysis RS data over a long period. In this regard, various big data processing platforms, such as Google Earth Engine (GEE), NASA Earth Exchange, Amazon’s Web Services, and Microsoft’s Azure have been developed [37]. In this regard, [38,39] illustrated the advantages and applications of GEE, including the fact that the number of publications is significantly increasing [39–41], GEE has been implemented on 70% of the world’s countries, and broad subjects have been studied [39]. So far, numerous studies have utilized GEE for LULC classification. For instance, Li et al. [42] exploited Sentinel-2 and Landsat-8 images to generate a 10 m map of the entire continent of Africa by a Random Forest (RF) classifier. Ghorbanian et al. [43] also leveraged Sentinel data to classify a large-scale area using RF at a 10 m spatial resolution and 13 LULC classes.

Currently, two European maps are available at a 10 m spatial resolution [19,25] (see Table 1). In [19], which was the first publication that classified the European continent at a spatial resolution of 10 m, multi-temporal Sentinel-2 images were only utilized for training an RF classifier. The LULC map was produced for the year 2017 in 14 classes. Despite the higher Overall Accuracies (OA) being obtained for several countries, the OA of the entire study area was 86%. Furthermore, ESA [44] follows a similar procedure to [19], incorporating Sentinel-1 images to provide global 10 m LULC yearly maps consisting of more than 12 classes. The project was inspired by the 2017 WorldCover conference [45], with an emphasis on developing innovative approaches. Finally, Venter and Sydneham [25] presented the most recent European 2018 LULC map -ELC10- using around 70,000 of the Land Use and Cover Area frame Survey (LUCAS) reference data and Sentinel-1/2 images, acquired in 2018. An OA of 90% was achieved using an RF classifier within the GEE platform. They have also discussed the robustness of RF and the minimal effect of Sentinel-2 atmospheric correction and Sentinel-1 speckle filtering to enhance the classification accuracy.

**Table 1.** Available 10 m LULC maps, covering the entire continent of Europe.

Name	Year	# Classes	Algorithm	Overall Accuracy	RS Data
FROM-GLC10 [20]	2017	10	RF	72%	Landsat-8, Sentinel-2
S2GLC [19]	2017	14	RF	86%	Sentinel-2
ELC10 [25]	2018	8	RF	90%	Sentinel-1, 2
Esri 2020 [26]	2020	10	CNN	85%	Sentinel-2
WorldCover 10 m [24,46]	2020	11	CatBoost	74%	Sentinel-1, 2

Moreover, three global maps have so far been generated at a spatial resolution of 10 m. Finer Resolution Observation and Monitoring of Global Land Cover (FROM-GLC10) [20] followed the existing 30 m resolution global land cover version [30]. An RF classifier was employed on Sentinel-2 images within GEE, where the OA was approximately 72%. Afterwards, an Esri 2020 LULC map was derived from Sentinel-2 images with an OA of 85% [26]. Ten LULC classes were categorized using a Deep Learning (DL) based segmentation model (i.e., UNet, with a Convolutional Neural Network (CNN) architecture) and

over 20,000 Sentinel-2 tiles on a Microsoft Planetary Computer. Following the WorldCover project, the ESA WorldCover 10 m 2020 map has been recently released [24,46]. Sentinel-1 and Sentinel-2 images were classified into 11 classes using the algorithm proposed by Buchhorn et al. [47]. This open-access global land cover map was generated from three separated workflows (i.e., data preprocessing, classification, and map generation), reaching a global OA of 74%. On the other hand, various maps were generated at a European national scale, such as Greece [48,49], France [50], Germany [51], Italy [52,53], and Belgium [54], which were not considered to be available maps in Table 1 due to the scale of the study areas and the spatial resolutions. Similarly, in this study, maps consisting of the entire continent of Europe but aimed at different applications and spatial resolutions were also neglected, such as global cropland maps [55,56], European-crop-type maps [17], pan-European land cover maps [18], and GlobeLand30 maps [57].

In addition to studies that have prepared LULC maps at the global or European scales, a wide range of articles have studied classification methods from pixel- and object-based points of view. Various pixel-based and object-based ML methods [58], semi-automated and automated classification techniques [59], along with different features retrieved from EOs [60], were utilized to generate LULC maps. For instance, Verde et al. [48] developed a classification workflow for fine-scale object-based land cover mapping for Greek terrestrial territory by evaluating several classification techniques and strategies for automatic and manual training data extraction. Previously, Stromann et al. [60] studied the impact of dimensionality reduction strategies on object-based SVM classification. They found that Sentinel-2 Normalized Difference Vegetation Index (NDVI), Normalized Difference Water Index (NDWI), and Sentinel-1 VV measurements were the most relevant features to optimize the SVM classifier and achieve higher classification accuracy. In this way, Qu et al. [58] investigated the performance of various auxiliary features in improving the accuracy of seven pixel-based and seven object-based RF classification models. Among all RF classification models analyzed by Qu et al. [58], the object-based methods showed higher overall accuracy than the pixel-based classification methods, as the best overall accuracy was achieved when the object-based method was used with spectral data only. Moreover, Tassi and Vizzari [61] focused on developing an object-oriented classification approach and the Simple Non-Iterative Clustering (SNIC) technique to find spatial clusters for creating cluster texture indices. Shafizadeh-Moghadam [62] also used SNIC and RF algorithms to produce a 30 m LULC map of the Tigris-Euphrates basin in the Middle East using Landsat-8 spectral and thermal bands, texture and spectral indices, and topographic factors. The study area was divided into five climate regions and the training samples were taken from each sub-region to increase the overall accuracy of the classification method.

This study initiated a sequential program to classify nine landmasses of 37 European countries using Sentinel-1/2, Landsat-8, and the LUCAS dataset within the GEE platform. So far, the integration of Sentinel-1/2 and Landsat-8 images has not been carried out to generate 10 m LULC maps at the global and European scales. The methodology is based on an object-based Artificial Neural Network (ANN), implemented on a large volume satellite image, acquired from 2016 to 2021. A novel reference data preparation was also proposed to take advantage of the least noisy samples by integrating two sources of LUCAS data and a data refinement procedure. This dataset has been mostly utilized without refining noisy samples in large-scale studies. In summary, the primary purpose of this work is to develop a procedure of generating accurate continental-scale LULC maps and addressing several issues in RS and in situ dataset preparation, leveraging European-based repositories (e.g., Sentinel images and LUCAS), the efficiency of cloud-based platforms in the processing of big geodata, and the state of main natural and artifact covers in Europe. In the following, the main contributions to the present paper regarding the proposed methodology are described:

- We integrated all Sentinel-1/2 and Landsat-8 images since 2016 to highly leverage spectral information and backscattering signals for generating a rich training model. Additionally, a data preparation procedure for the LUCAS dataset was proposed

to avoid uncertainties and misclassifications in the final map. The repository also contained the provider raw data and previous studies' refined LUCAS data to exploit available reference samples thoroughly.

- A heterogeneous feature map was generated from three segmented images extracted from Sentinel-1/2 and Landsat-8 features using the SNIC algorithm to reduce the usual LULC mapping noises and enhance the reliability of the final LULC map. The heterogeneous feature map was created using an NDVI time series of Sentinel-2 and Landsat-8 images and bi-monthly VV/VH images of Sentinel-1 after the preprocessing of images.
- We tailored an object-based ANN model in a fully connected architecture to learn 16 input features of the heterogeneous feature map and training/validation datasets within the Google Colab. Afterwards, we implemented rule-based post-processing using the slope and water index to reduce the associated uncertainty and increase the accuracy of several classes through knowledge-based criteria.

This paper is structured as follows. First, a general overview of the study area, seven European biogeographical regions, and satellite images are introduced. A comprehensive explanation of the LUCAS dataset is then provided, including the history of this survey, the description of nine LULC classes, the propagation of the samples, and the portion of each class in seven ecozones. The methodology section comprehensively describes the satellite data preparation, the reference samples preparation, the object-based image segmentation algorithm, the classification process, the post-processing method, and accuracy assessment. The result section consists of the 10 m European LULC map, ELULC-10, classification results analysis, and a discussion of the outcomes. The paper ends with a general discussion of the results, limitations, recommendations for future studies, and the conclusion.

## 2. Study Area and Data

### 2.1. Study Area

The study area included 37 countries based on European Environment Agency (EEA) instruction, including 27 European Union member states and the United Kingdom, Liechtenstein, Norway, Switzerland, and six Western Balkan countries. The study area had a high ratio of coast to landmass and significant land relief variation temperate climate zones, divided into four topographic regions (Western Uplands, North European Plain, Central Uplands, and Alpine Mountains). The climate varied widely across the seven main biogeographical regions, as shown in Figure 1 (ordered from the smallest to the largest): Steppic (0.76%), Pannonian (3.03%), Alpine (13.27%), Atlantic (17.32%), Boreal (18.2%), Mediterranean (18.93%), and Continental (28.5%). The dominant vegetation cover was mixed forest, and the growing season varied between 100 days and 200 days from north to south. Moreover, Corine Land Cover (CLC) 2018 reported that the study area covered around 6 million km<sup>2</sup> composed of 48.80% forest and semi-natural areas, 41.80% agricultural areas, 4.30% artificial surfaces, 2.6% water bodies, and 2.50% wetlands (CLC 2018). More than half of the European countries dedicated about 40% to agricultural lands, including arable land, heterogeneous agricultural areas, pastures, and permanent crops. It is worth noting that these statistics are based on CLC 2018, with a minimum linear element width of 100 m [63].



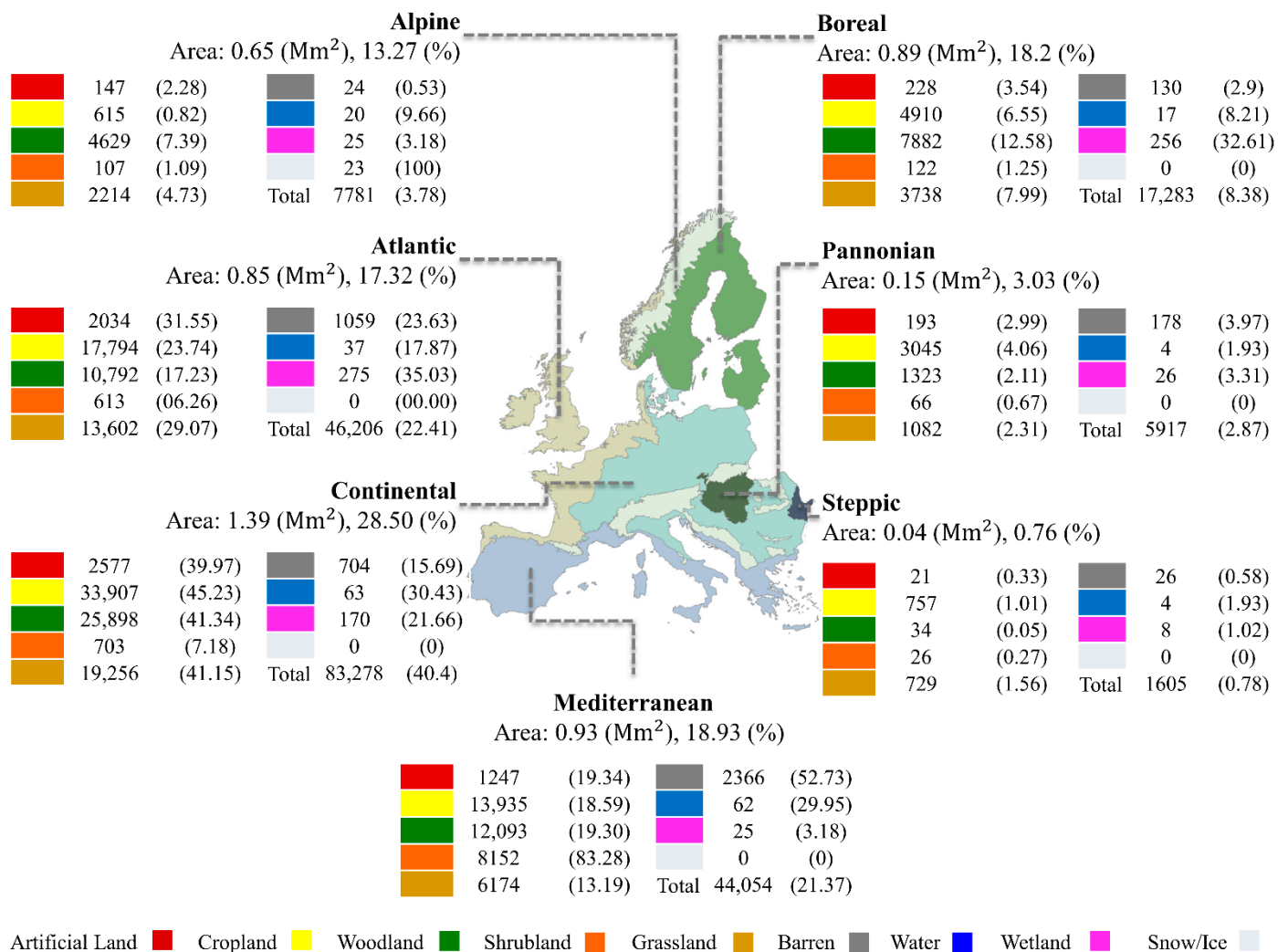


**Figure 1.** The number of each sample in European biogeographical regions and percentage (within parentheses) of each class to the total number of the correspondent class, along with the area (Mm<sup>2</sup>, %) of the biogeographical regions.

## 2.2. Datasets

### 2.2.1. Sentinel-1

The Sentinel-1 mission operates a dual-polarization C-band synthetic aperture radar (SAR) imaging during day and night, enabling them to acquire imagery regardless of the weather. In 12 days, Sentinel-1 revisits the same coverage as Sentinel-2, while the repeat cycle is 6 days over Europe. The GEE database provides processed Sentinel-1 Ground Range Detected (GRD) scenes in three instrument modes of IW (Interferometric Wide Swath), EW (Extra Wide Swath), and SM (Strip Map), which contain either one of three spatial resolutions (10, 25 or 40 m) and one or two out of four band combinations (Vertical-Vertical (VV): single co-polarization, Horizontal-Horizontal (HH): single co-polarization, VV + VH: dual-band cross-polarization, and HH + HV: dual-band cross-polarization), depending on the instrument's polarization settings. The Sentinel-1 GRD products were already ortho-rectified and converted to the backscattering coefficient ( $\sigma^0$ , dB). They underwent five steps: (1) orbit correction, (2) GRD border noise removal, (3) thermal noise removal, (4) radiometric calibration, and (5) terrain correction, the detail of which are provided in [64]. For this study, 18,740,310 m Sentinel-1 images were used to cover the study area.

### 2.2.2. Sentinel-2

The Copernicus Sentinel-2 systematically covers more than 90% of the world, including all continental land surfaces (including inland waters) between the latitudes of 56° South and 84° North, all coastal waters up to 20 km from the shore, all islands greater than 100 km<sup>2</sup>, all EU islands, the Mediterranean Sea, and all closed seas (e.g., the Caspian Sea). The twin satellites of Sentinel-2 regularly revisit all continental land surfaces with a high revisit frequency of five days. The optical instrument payload of Sentinel-2 consists of 13 spectral bands: four bands at a 10 m spatial resolution (Blue (2), Green (3), Red (4), and NIR (8)), six bands at 20 m (Red edge1 (5), 2 (6), and 3 (7), Narrow Near Infrared (8A), SWIR1 (11), and SWIR2 (12)), and three bands at 60 m (Aerosols (1), Water vapor (9), and Cloud mask (10)) spatial resolution. In this study, 138,441 images at bands 2, 3, 4, and 8 from 2016 to 2021 were used.

### 2.2.3. Landsat-8

Landsat-8 is a multi-spectral satellite launched by the United States Geological Survey (USGS) in 2013. This study utilized Landsat-8-calibrated surface reflectance products with 11 spectral bands. The spectral bands included 30 m coastal aerosol (band 1), 30 m visible (band 2–4), 30 m Near Infrared (NIR, band 5), 30 m Shortwave Infrared (SWIR, band 6–7), 15 m panchromatic (band 8), 15 m cirrus (band 9), and 100 m thermal infrared (band 10–11) bands. Overall, 9331 Landsat-8 images were extracted in this study to mainly derive various spectral indexes for the LULC mapping task. Figure 2 shows the number of Sentinel-1/2 and Landsat-8 images from 2016 to 2021 above the entire continent of Europe, utilized as input data in the proposed methodology.

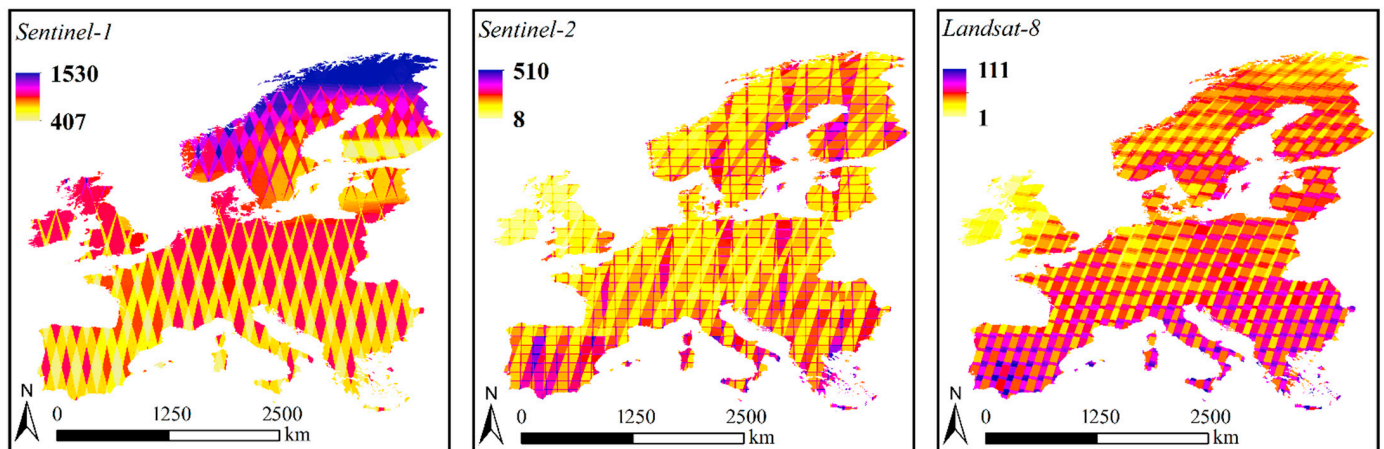


**Figure 2.** The number of Sentinel-1/2 and Landsat-8 images over the study area.

### 2.2.4. ASTER and SRTM

Digital Elevation Model (DEM) data was also incorporated with three other remote sensing data sources to enhance the final classification results. A DEM is a raster-based data source in which each pixel value represents the corresponding altitude above sea level, which is considered to be a primary attribute of the Earth's surface. In this paper, DEM data from two remote sensing sources were employed. The first DEM has been derived from the Advanced Spaceborne Thermal Emission and Reflection Radiometer (ASTER). The ASTER instrument has the capability of acquiring images through its back-ward-looking telescope and thus can provide along-track stereo pairs. These pairs are processed using standard photogrammetric approaches and a detailed camera model to produce DEM data with approximately 30 m spatial resolution [65]. The second DEM data has been produced from the Shuttle Radar Topography Mission (SRTM). The SRTM has been generated through the Interferometry of Synthetic Aperture Radar (InSAR) technique with dual antennas during the same pass [66]. Here, the SRTM version 3 data with approximately 30 m spatial

resolution, which has been subjected to void-filling approaches for quality enhancement, was used.

#### 2.2.5. LUCAS Reference Data Repository

Land Use and Cover Area frame Survey (LUCAS) provides harmonized information on land use, land cover, and environmental parameters to provide European-wide agriculture, environment, and countryside analysis, and validate RS-based LULC maps [51]. Every three years since 2006, the European Statistical Office (Eurostat) has carried out LUCAS surveys. LUCAS 2018 was the latest survey conducted in the spring-summer of 2018 over 28 EU countries (including the United Kingdom), following five principles: spatial consistency, temporal consistency, compatibility with existing systems (e.g., Farm Structure Survey (FSS), European Classification of Economic Activities (NACE), Food and Agriculture Organization (FAO), and Infrastructure for Spatial Information in Europe (INSPIRE)), independence from observation methods, and no gaps and no overlaps. The LULC conditions of the LUCAS sampling approach dataset assess in situ on a relatively high-density grid, while the Copernicus program (CORINE) focuses on RS approaches. LUCAS in situ samples were extensively employed in relevant disciplines, such as CORINE validation [67,68], area estimation in geographic units [69], the validation of available reference data over EU [70] and Greece [71], the differentiation of cropland and grassland over Germany [72], the generation of a new LULC product for Germany [51], automated LULC classification over EU with open geodata [73], and mapping EU land cover using spectral-temporal metrics [18].

The latest LUCAS survey, conducted in 2018 [74], was selected in this study to train and validate the produced European LULC map. Among six open-access pan-European geodata sets (i.e., CORINE, Natura 2000, Riparian Zones, Urban Atlas, OpenStreetMap, and LUCAS), it has the largest and most comprehensive land cover database in Europe [69]. The LUCAS surveys separate classification systems for land cover (the physical cover of the Earth's surface) and land use (the socio-economic function of the land) into eight main categories (i.e., artificial land, cropland, woodland, shrubland, grassland, bare land and lichens/moss, water areas, and wetlands). It provides observations at 337,854 points surveyed in the EU Member States from March 2018 to November 2018. In 2018, the LUCAS survey was carried out in 28 European countries, where LUCAS points were either visited by field surveyors or photo-interpreted in the office. For the statistical sample of the LUCAS survey, a regular 2 km grid with over 1,100,000 points was overlaid on the EU territory. Since LUCAS is a point survey, the size of the point in the real world needed to be defined. Therefore, a circle with a variable radius from 1.5 m to 20 m was specified as the sampling unit. A harmonized version of the LUCAS dataset has also been provided [75] to overcome several drawbacks in the original datasets, such as inconsistencies between legends and labels, as well as missing internal cross-references. Finally, a multi-year harmonized database was created using the five surveys (in 2006, 2009, 2012, 2015, and 2018) [75].

In this study, 206,147 field samples were included in nine classes from the latest-released version of LUCAS 2018, in February of 2020, and the harmonized version in November 2020 (see Table 2). These datasets were used to carry out a validation ANN procedure, as described in the methodology section. Since the GPS precision of 100,120 samples was not reported, in this study those points were removed from the analysis. In total, 70% of the in situ reference repository was randomly divided into training samples to train the ML algorithm. Moreover, Figure 1 presents each class number in different biogeographical regions and their ratio to the total number of correspondent classes. It also contains the area of biogeographical regions and the percentage of each region over the study area. Continental and Steppic regions contain the most and least training and test samples.

**Table 2.** The description and number of nine LUCAS classes and subclasses.










Propagation	LULC Class	LUCAS Description	# Sub Classes	# Samples (%)
	Artificial Land	Areas characterized by an artificial and often-imperious cover of constructions and pavement (A00).	5	6447 (3.13)
	Cropland	Areas where crops are planted and cultivated (B00).	137	74,963 (36.36)
	Woodland	Areas covered by trees with a canopy of at least 10%. In addition, woody hedges and palm trees are included in this class (C00).	21	62,651 (30.39)
	Shrubland	Areas dominated (at least 10% of the surface) by shrubs and low woody plants that are normally not able to reach more than 5 m in height. It may include sparsely occurring trees with a canopy below 10% (D00).	2	9789 (4.75)
	Grassland	Land predominantly covered by communities of grassland, grass-like plants and forbs. This class includes permanent grassland and permanent pasture that is not part of a crop rotation (normally for 5 years or more), which can be used to grow grasses and other herbaceous forage naturally (self-seeded) or through cultivation (sown). It may include sparsely-occurring trees within a limit of a canopy below 10% and shrubs within a total limit of cover (including trees) of 20%. These can, themselves, also be grazed, provided that grasses and other herbaceous forage remain predominant as well (E00).	3	46,795 (22.70)
	Barren	Areas with no dominant vegetation cover on at least 90% of the area or areas covered by lichens/moss (F00).	4	4487 (2.18)

Table 2. Cont.

Propagation	LULC Class	LUCAS Description	# Sub Classes	# Samples (%)
	Water	Inland or coastal areas without vegetation and covered by water and flooded surfaces, or likely to be so over a large part of the year. If temporarily dry, the outlines of the water areas have to be clearly visible on the orthophotos. Temporarily submerged islands and sandbanks are to be assigned in FXX classes, with a remark “temporarily flooded” (G00). In this study, 23 samples of Glaciers, Permanent Snow (G50) were moved to Sea/Ice class.	7	207 (0.10)
	Wetland	Wetlands are areas that fall between land and water. These are areas that are wet for long enough periods that the plants and animals living in or near them are adapted to, and often dependent on, wet conditions for at least part of their life cycle (H00). Wetlands are defined as land that is: (a) Inundated with water on a temporary or permanent basis, (b) Inundated with water that is usually slow moving or stationary, (c) Inundated with water that is shallow, or (d) Inundated with water that may be fresh, brackish or saline.	5	785 (0.38)
	Snow/Ice	“Glaciers, Permanent Snow” (G50) is a sub class of Water. These areas are covered by glaciers (generally measured at the time of their greatest expansion in the season) or permanent snow.	0	23 (0.01)

### 3. Methodology

Figure 3 presents the flowchart of the proposed classification method for continental Europe LULC mapping. Each step is also explained in detail in the following subsections.

#### 3.1. Data Preparation

##### 3.1.1. Satellite Data Preprocessing

As stated earlier (see Section 2.2), three types of satellite datasets were employed to produce the continental scale map of Europe. The preprocessing steps applied to each satellite data are explained below.

A Sentinel-1 GRD dataset at IW mode, accessible within GEE through the snippet of *ee.ImageCollection* (“COPERNICUS/S1\_GRD”), was employed to generate SAR features. All Sentinel-1 images were grouped into six two-month intervals (see Table 3) and then were aggregated using the *mean reducer* function to produce bi-monthly SAR features. This step allowed the production of SAR features with lower susceptibility to image acquisition conditions. It also reduced speckle noise from the mosaicked images [76]. Consequently, 12 SAR features (i.e., six bi-monthly VV and six bi-monthly VH) were generated for further processing. It is worth noting that incorporating bi-monthly SAR features could beneficially contribute toward separating different classes in the study area by preserving temporal features [77,78].



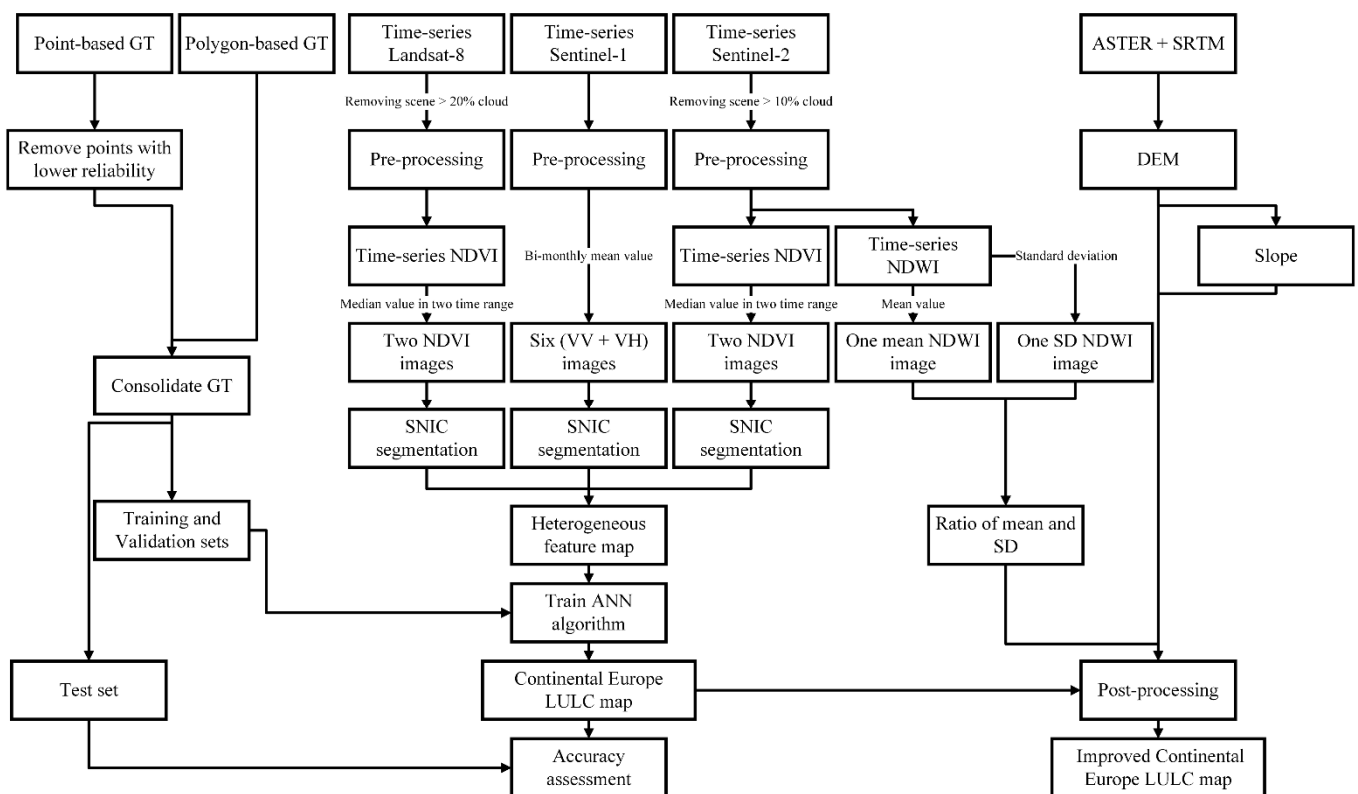


**Figure 3.** The flowchart used for generating the ELULC-10 map (GT: Ground Truth as LUCAS reference samples, ASTER: Advanced Spaceborne Thermal Emission and Reflection Radiometer, SRTM: Shuttle Radar Topography Mission, DEM: Digital Elevation Model, NDVI: Normalized Difference Vegetation Index, NDWI: Normalized Difference Water Index, SNIC: Simple Non-iterative Clustering, SD: Standard Deviation, ANN: Artificial Neural Network, and LULC: Land Use Land Cover).

**Table 3.** The number of satellite images from 2016 to 2021 (e.g., Sentinel-1, -2, and Landsat-8) utilized for providing features after the preprocessing procedure.

Month		Satellite Datasets					
		Sentinel-1		Sentinel-2		Landsat-8	
		Features	# Image	Features	# Image	Features	# Image
1	January	VV-1, VH-1	30,709	×	×	×	×
2	February			×	×	×	×
3	March	VV-2, VH-2	31,871	×	×	×	×
4	April						
5	May	VV-3, VH-3	24,579	NDVI-1	55,388	NDVI-1	3987
6	Jun						
7	July	VV-4, VH-4	34,159				
8	August			NDVI-2	83,053	NDVI-2	5344
9	September	VV-5, VH-5	34,530				
10	October						
11	November	VV-6, VH-6	31,555	×	×	×	×
12	December			×	×	×	×
Total		6 VV, 6 VH		2 NDVI		2 NDVI	

Sentinel-2 level-2A products, accessible within GEE through the snippet of *ee.ImageCollection* ("COPERNICUS/S2\_SR"), were utilized for the classification task. These products provide surface reflectance values, and are derived from the Sentinel-2 level-1C dataset by applying the Sen2Cor prototype processor [79]. This processor performs atmospheric, terrain, and cloud (i.e.,

cirrus) corrections, and creates Sentinel-2 level-2A products with ready-to-use data for different applications. Furthermore, due to the sensitivity of optical data to the presence of clouds, all Sentinel-2 images with cloud cover higher than 10% were excluded from further analysis. Additionally, the quality band of each image was incorporated to eliminate invalid observations and produce cloud-free optical images. Afterwards, the red and NIR bands of Sentinel-2 images were incorporated to calculate the NDVI for all considered images. Subsequently, the generated NDVI images were grouped into two intervals (see Table 3), and the *median reducer* function was then applied to downscale Sentinel-2 NDVI images. The *median reducer* allowed the generation of homogenous optical data over the study area in which cloudy, very bright, and very dark pixels were removed [43,80]. Consequently, two NDVI images from Sentinel-2 level-2A datasets were considered for further processing.

Landsat-8 level-2 products, accessible within GEE through the snippet of *ee.ImageCollection* ("LANDSAT/LC08/C02/T1\_L2"), were used as another source of optical data. These products included atmospherically corrected surface reflectance values, which have been derived by applying the Land Surface Reflectance Code (LaSRC) algorithm [81,82]. Similar to Sentinel-2 images, a cloud cover filtering step was applied to remove the Landsat-8 datasets with a cloud cover of over 20%. Later, the pixel quality band of each image was employed to remove invalid observations and to produce cloud-free optical images. Afterwards, the NDVI images of all considered Landsat-8 datasets were produced (see Table 3) and then were downscaled by applying the *median reducer* function. The *median reducer* function allowed the generation of homogenous optical data over Europe in which cloudy, very bright, and very dark pixels were removed [43,80]. Accordingly, two NDVI images from Landsat-8 level-2 datasets were considered for further processing.

Overall, a combination of twelve SAR features (i.e., six VV and six VH) and four NDVI images (i.e., two Sentinel-2 NDVI images and two Landsat-8 NDVI images) were used as input features to perform the LULC classification task (see Table 3).

### 3.1.2. Reference Samples Preparation

In this study, two reference datasets generated pointwise (LUCAS 2018 [74]) and with polygon (harmonized version [75]) units were employed. As described earlier in Section 2.2.4, the first reference dataset contained more samples in pixel units with a better distribution across the European lands, with a portion of samples with lower reliability that could negatively affect the classification procedure. In contrast, the second reference dataset included fewer samples in polygon units with higher precision. Therefore, it was inevitable to implement a preprocessing step to exclude samples with lower reliability from the first reference dataset. Thereafter, the remaining samples of the first reference dataset were merged with the second reference dataset to produce a consolidated reference dataset. To this end, the first reference dataset was initially divided into five independent subsets. Each subset was then individually applied to train and validate several independent ANN algorithms (described ahead in Section 3.3). In this regard, five soft (i.e., output rule images of the ANN classifier) classification results were calculated, wherein pixel values showed the probability of occurrence of the corresponding pixel to each class (i.e., nine LULC classes). Since the label of reference samples was already known, Equation (1) was adopted to remove reference samples with lower reliability.

$$Reliability\ Measure = \frac{\sum_{i=1}^5 P_i^{True}}{\sum_{i=1}^5 P_i^{max}} \quad (1)$$

in which  $i$  indicates the  $i$ th classification result from the  $i$ th subset,  $P_i^{True}$  is the probability of true class in the  $i$ th classification result, and  $P_i^{max}$  is the maximum probability of the corresponding pixel in the  $i$ th classification result. The value of Equation (1) reaches one when, in all classification results, the true class probabilities are equal to the maximum probabilities. Conversely, its value reaches to zero when the assigned class (i.e., maximum probability) does not match the true class (i.e., probability of true class) in all five classifica-

tion results. Finally, a threshold value of 0.2 was considered to exclude reference samples with lower reliability. The remaining samples were preserved and merged with reference samples of the second reference dataset for further analysis.

### 3.2. Segmentation

Previous studies acknowledged the higher efficiency of object-based image analysis to improve the accuracy and quality of the generated LULC maps [83–87]. Accordingly, the Simple Non-Iterative Clustering (SNIC) algorithm, available as a prominent segmentation algorithm within GEE, was used to segment preprocessed satellite datasets. SNIC is a modified version of the Simple Linear Iterative Clustering (SLIC) segmentation algorithm that was improved by removing the iterative procedure and enforcing the connectivity constraints from the initial step [88]. This segmentation algorithm is started by a user-defined number of seed points scattered on a regular grid across the image space. Later, a five-dimensional distance measure (i.e., spatial coordinates and CIELAB color space) along with the 4/8 connectivity constraint are applied to grow each seed point region, resulting in the final segmentation image. The implemented SNIC segmentation algorithm within GEE includes five input parameters: size, compactness, connectivity, neighborhood size, and seeds, the first four of which are mandatory and should be determined by the user [89]. In this study, the SNIC algorithm was applied to each preprocessed satellite dataset (see Section 3.1.1) separately, resulting in three segmentation outputs. To this end, the input parameters of the SNIC algorithms were set to 50 (Size), 1 (Compactness), 8 (Connectivity), 100 (Neighborhood Size), and null (Seeds), which were determined through several trial-and-error attempts to find optimum values. Subsequently, three segmentation results were merged through a heterogeneous feature map analysis to generate the final segmentation result with a higher accuracy for further analysis [90]. The heterogeneous features fusion strategy is a step to construct the final informative representation of multiple sets of satellite images [91]. The heterogeneous features at data-level mean that various features with inherent differences are inputted to the classification algorithm [91]. In this study, the heterogeneous feature map was constructed with finer segments by overlaying different coarse segments of the input bands. The performance of fusing coarse-segmented features was previously shown in cropland classification [92]. It also demonstrated a high accuracy in land cover time-series analysis [86]. The final segmentation results were used to average the corresponding pixel values (i.e., in all input features) to reduce the noise (i.e., the salt and pepper effect of the pixel-based classification) and increase the reliability of the produced LULC map [60,92].

### 3.3. Classification

Inspired by the biological neurons system, ANN algorithms are among the most widely used supervised ML algorithms [93–96]. Interconnected artificial neurons are the central components of ANN that simulate the neural processing of the human nervous recognition system and have a high potential to solve non-linear problems, such as classification tasks [92,97].

In this study, the final mosaicked image with 16 features was employed to produce the LULC map of Europe. As mentioned earlier (see Section 2.2.4), the consolidated reference dataset after the preprocessing step (see Section 3.1.2) was randomly divided into three independent subsets of training (70%), validation (15%), and test (15%) samples. Subsequently, the training and validation samples were respectively used to train and adjust the parameters of the ANN algorithm. Later, the independent test samples were incorporated to perform statistical accuracy assessment and evaluate the performance of the implemented approach. Despite the high computation capabilities and advantages of GEE, currently, this cloud platform does not support ANN algorithms in its JavaScript API, and thus, further analysis was applied within the Google Colab with a direct linkage to GEE.

ANN algorithms with different architectures have been developed to produce LULC maps [92,94,95,97,98]. Accordingly, the first step to implement an ANN algorithm is determining the required parameters to define the ANN architecture identically. To this end, four parameters: (1) the number of layers, (2) the number of neurons, (3) the type of activation function, and (4) the learning algorithm, should be determined. Accordingly, in this study, a fully connected ANN architecture with an input layer containing 16 neurons (i.e., equal to the number of input features), two hidden layers with 100 and 50 neurons, respectively, and one output layer with 9 neurons (i.e., equal to the number of classes) were employed. The activation functions in the hidden layers and the output layer were sigmoid and SoftMax, respectively. Furthermore, the adaptive moment estimation (Adam) method was used as the back-propagation learning algorithm [99]. Additionally, the cross-entropy loss function was employed as the stopping criteria, and the ANN algorithm satisfied this criterion after 200 iterations. It is worth noting that the parameter determination step was conducted based on the visual interpretation of the results of the classification, as well as using validation samples to have statistical measures. Finally, the trained ANN algorithm was applied to the final mosaicked image with 16 features to produce the European LULC map.

### 3.4. Post-Processing

After applying the classification algorithm (see Section 3.3), a post-processing step was also implemented to improve the generated LULC map. This aimed to reduce the associated uncertainty and to increase the accuracy of several classes through knowledge-based criteria. In this regard, the Digital Elevation Models (DEM) from ASTER (northern part of Europe) and SRTM (southern part of Europe) were first utilized to delineate high elevation locations to enhance the classification results of the Snow/Ice class. In this regard, two threshold values of 1300 (in Sweden and Norway) and 2100 (remnant parts of Europe) were considered to delineate the potential locations and convert them into polygon format. Later, a visual inspection of high-resolution images, available in Google Earth, was used to manually refine the delineated polygons. Then, these corrected polygons were applied, as a binary mask, to the generated LULC map to remove the wrongly classified objects in mountainous areas with a high potential of ice and snow cover. Second, the slope (i.e., calculated from DEM datasets) and NDWI images were simultaneously incorporated to enhance the quality of the Water, Barren, and Artificial Land classes. To this end, the annual NDWI images were calculated using all Sentinel-2 images, and then, the ratio of annual mean NDWI to the standard deviation of annual NDWI images was computed for each object. In this ratio index, the higher values belonged to permanent water areas, while lower values were related to other classes (i.e., Barren and Artificial Land in this case). This was due to the fact that water pixels had high NDWI values and a low standard deviation considering the annual NDWI images. Subsequently, two thresholds of NDWI more than 0.8 and slope values of over 15 degrees were set to refine the classification results of Water, Barren, and Artificial Land. In other words, these two datasets were incorporated to reduce the misclassifications that occurred between Water and two classes of Barren and Artificial Land.

### 3.5. Accuracy Assessment

Three different strategies were applied to assess the accuracy of the produced European LULC map. First, a visual inspection was conducted to compare the final classification results with the available very high-resolution satellite images within ArcMap for different regions. To this end, several random locations with diverse LULC classes were considered for comparison, assuring the high reliability of the produced LULC map. Statistical analysis was also performed to compute the statistical accuracy measures of the produced LULC map. Regarding the statistical accuracy assessment, different confusion matrices were calculated, and then, several metrics, including OA, Kappa Coefficient (KC), Producer Accuracy (PA), and User Accuracy (UA), were derived. It should be noted that the confusion

matrices were calculated once for the whole European LULC map, as well as for seven other different ecoregions in Europe. This procedure allowed a comprehensive evaluation of the produced continental-scale LULC map of Europe. Finally, as the third strategy, the produced LULC map was compared with other existing LULC maps of Europe to reveal the applicability of the developed approach.

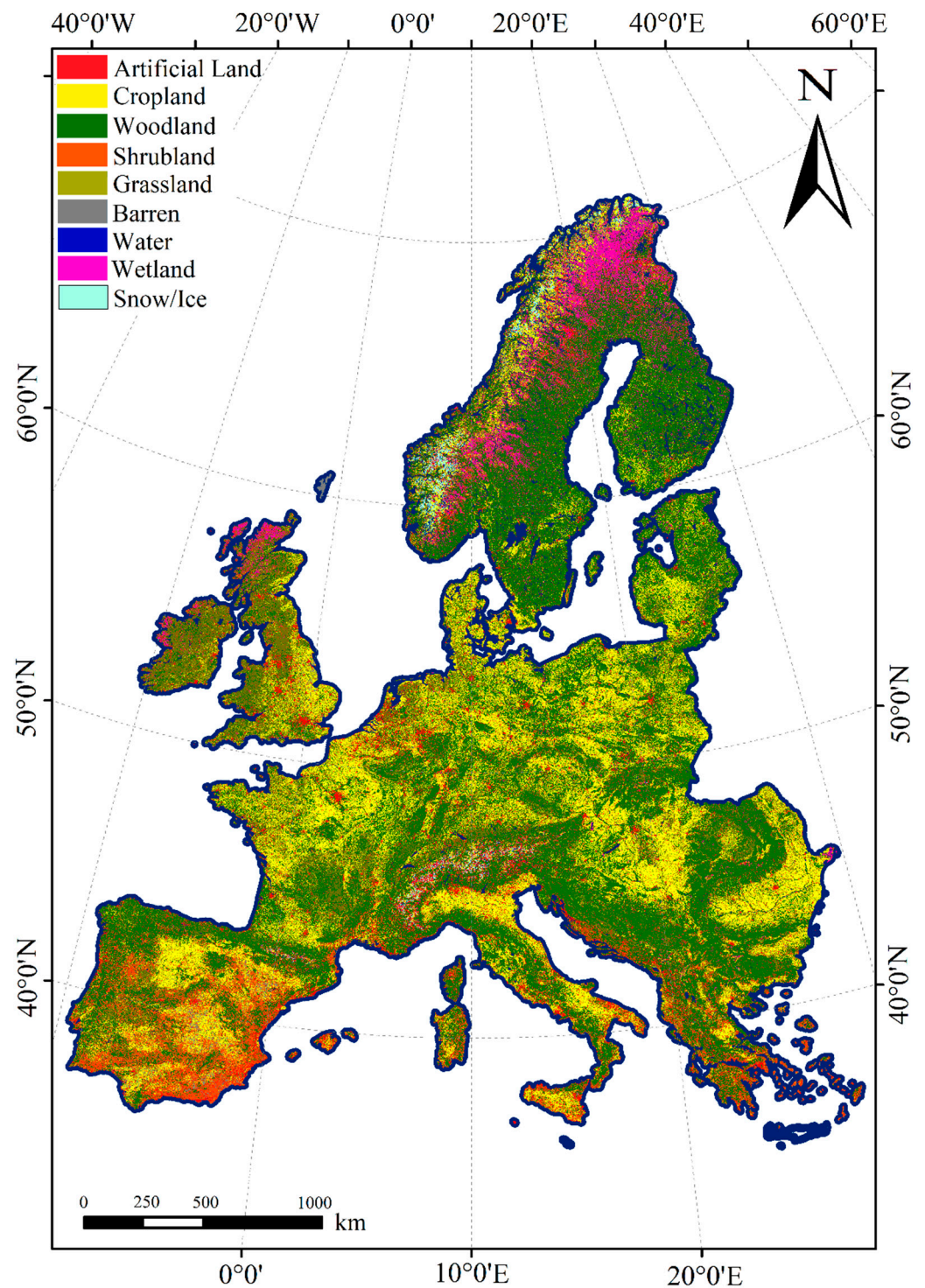
#### 4. Results

Figure 4 illustrates the produced European-wide LULC map at a 10 m spatial resolution using the ANN classification and LUCAS 2018 datasets in the GEE platform. The results also demonstrate the high potential of the proposed approach within GEE to identify LULC classes accurately in a diverse continent, like Europe. As shown in Table 4, the classification algorithm obtained 95.38% OA and 0.94 KC across Europe, where the minimum and maximum OAs were derived in the Mediterranean (90.20%) and Alpine (97.21%), respectively. Table 4 also provides the confusion matrix of the proposed methodology, including the UAs and PAs of nine LULC classes. Artificial Land, Woodland, and Water were classified with the highest accuracies (i.e., PA and UA were over 97%). Although most of the classes were mapped with over 87% accuracies, Barren samples were confused with those of Croplands. For example, around 27% of the Barren samples were wrongly classified as Cropland, which could be justified as a seasonality effect. Most Cropland areas are not cultivated for several months, generating confusion with Grassland and Barren classes. Furthermore, Barren areas are highly distributed across Europe and cover only 1.22%, limiting the identification of Barren with a high accuracy. Moreover, thanks to Sentinel-1 data availability, Snow/Ice was accurately detected in Alpine areas (95.65%). The SAR polarized data made it possible to distinguish this class, along with the capability of free cloud imaging over Snow/Ice coverages, which are masked mainly by clouds in optical images during most days of the year.

**Table 4.** The confusion matrix of the post-processed ELULC 10 map, along with OAs and KCs of all classes in seven biogeographical regions.

Classes		Predicted Samples									
		1	2	3	4	5	6	7	8	9	PA (%)
Reference data	1 Artificial Land	6389	40	19	16	26	13	0	0	0	98.25
	2 Cropland	49	71,938	487	464	1965	368	2	8	0	95.56
	3 Woodland	18	202	61,174	852	487	152	3	24	0	97.24
	4 Shrubland	3	61	496	8854	350	80	1	19	0	89.76
	5 Grassland	26	1078	375	361	45,012	125	3	35	0	95.74
	6 Barren	33	1237	38	50	43	3097	7	0	1	68.73
	7 Water	0	0	1	2	1	1	205	0	0	97.62
	8 Wetland	0	4	3	5	37	49	1	720	0	87.91
	9 Snow/Ice	0	0	0	0	0	1	0	0	22	95.65
	UA (%)	98.03	96.48	97.73	83.50	93.93	79.70	92.34	89.33	95.65	
		Alpine	Atlantic	Boreal	Continental		Mediterranean		Pannonian	Steppic	Europe
OA		97.21	95.85	96.09	93.98		90.20		96.46	96.09	95.38
KC		0.95	0.93	0.94	0.91		0.87		0.93	0.92	0.94





**Figure 4.** ELULC 10 of the year 2021 produced by an object-based SNIC model and ANN models in nine classes.

Figure 5 indicates PAs, UAs, Average of Producer Accuracy (APA), and Average of User Accuracy (AUA) in all biogeographical regions and for all LULC classes except Snow/Ice because this class only exists in the Alpine ecozone. It may be asserted that the majority of the classes were classified accurately. Additionally, the AUAs and APAs ranged between 60–97% and 45–94%, respectively, for the nine LULC classes. The highest accuracy was obtained for Water (100%) in the Atlantic, Pannonian, and Steppic regions. However, Barren and Shrubland were classified with less than 40% PA in the Boreal ecozone,

which seemed to be due to data availability (i.e., only 1.25 and 2.9 portions of reference samples, respectively) and land cover characteristics. On the other hand, there was no substantial bias in classifying the most dominant biogeographical regions (e.g., Continental and Mediterranean) and classes (e.g., Woodland and Cropland), which demonstrated the proposed methodology's capability to identify spectral differences.

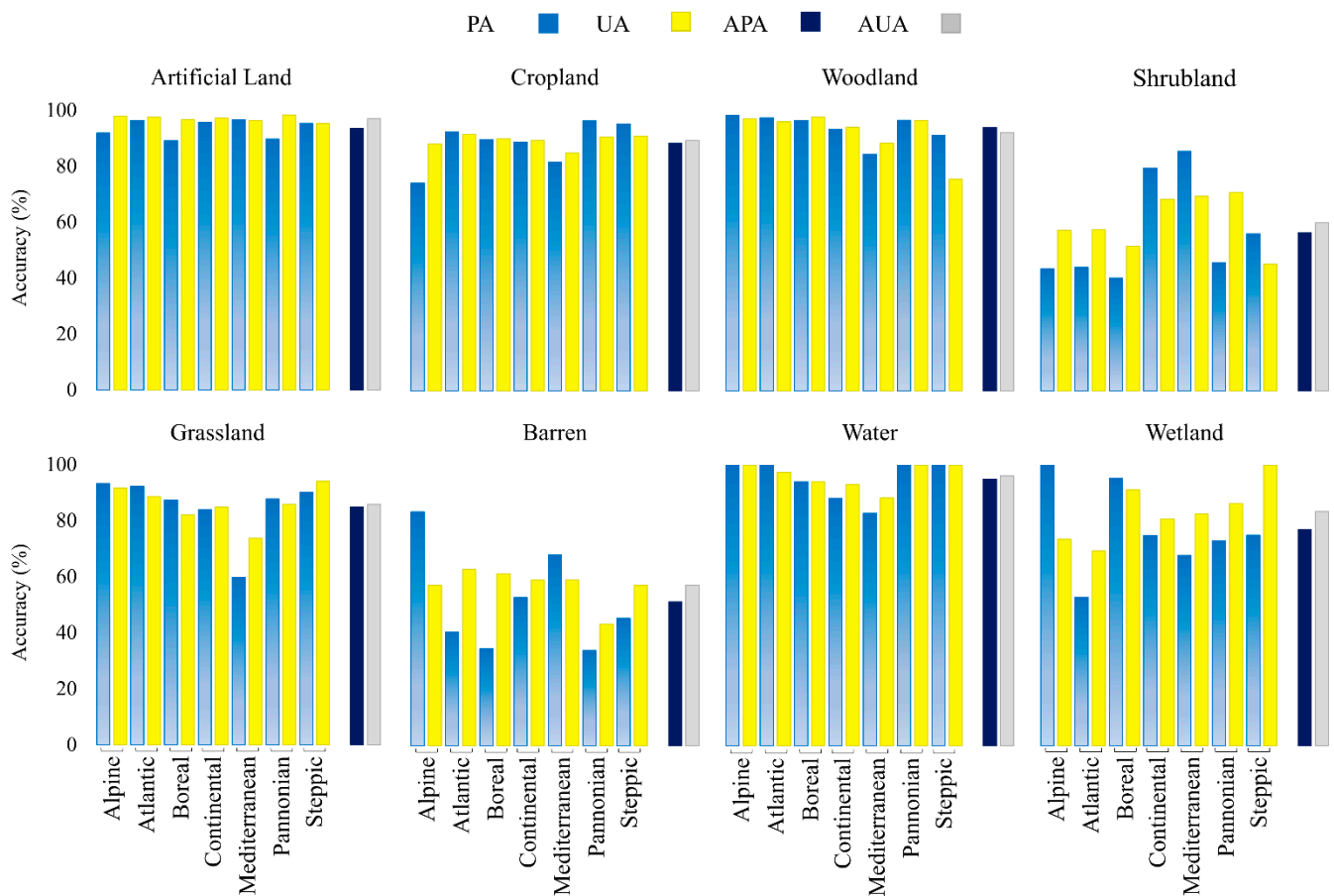


**Figure 5.** The accuracies report of all classes in all biogeographical regions, including OA, PA, UA, Average of Producer Accuracy (APA), and Average of User Accuracy (AUA) before post-processing.

Among the classes with less than 10% coverage, Artificial Land showed the highest accuracies (APA = 93.50% and AUA = 97%), followed by Water (APA = 95.01% and AUA = 96.12%). Both classes were accurately identified in all seven biogeographical regions. The results highlight the proposed methodology's efficiency in distinguishing small and heterogeneous built areas and diverse edges of water bodies, such as rivers and lakes. Moreover, the accurate prediction of Wetland areas (PA = 96.15% and UA = 86.21%) in Alpine, which is the most common place of wetlands, might show the impact of using SAR images in accurate Wetland classification.

The European LULC map provides particular interests for various applications demanding generalized LULC details, such as agriculture, forestry, urban studies, and hydrology. Figure 6 highlights the extent of all classes across Europe with a 10 m binary mask. These maps confirm that the green natural areas, Woodland (40.27%) and Cropland (22.42%), are the most prevalent in Europe, similar to what was reported in CLC 2018. On the other hand, the Barren and Snow/Ice classes have the least coverage. This figure also indicates the distribution of each class. For instance, the high density of Woodland and isolated Shrubland areas could be detected in the northern regions and south western regions of Spain, respectively. Likewise, most Wetland areas were over the northern regions.

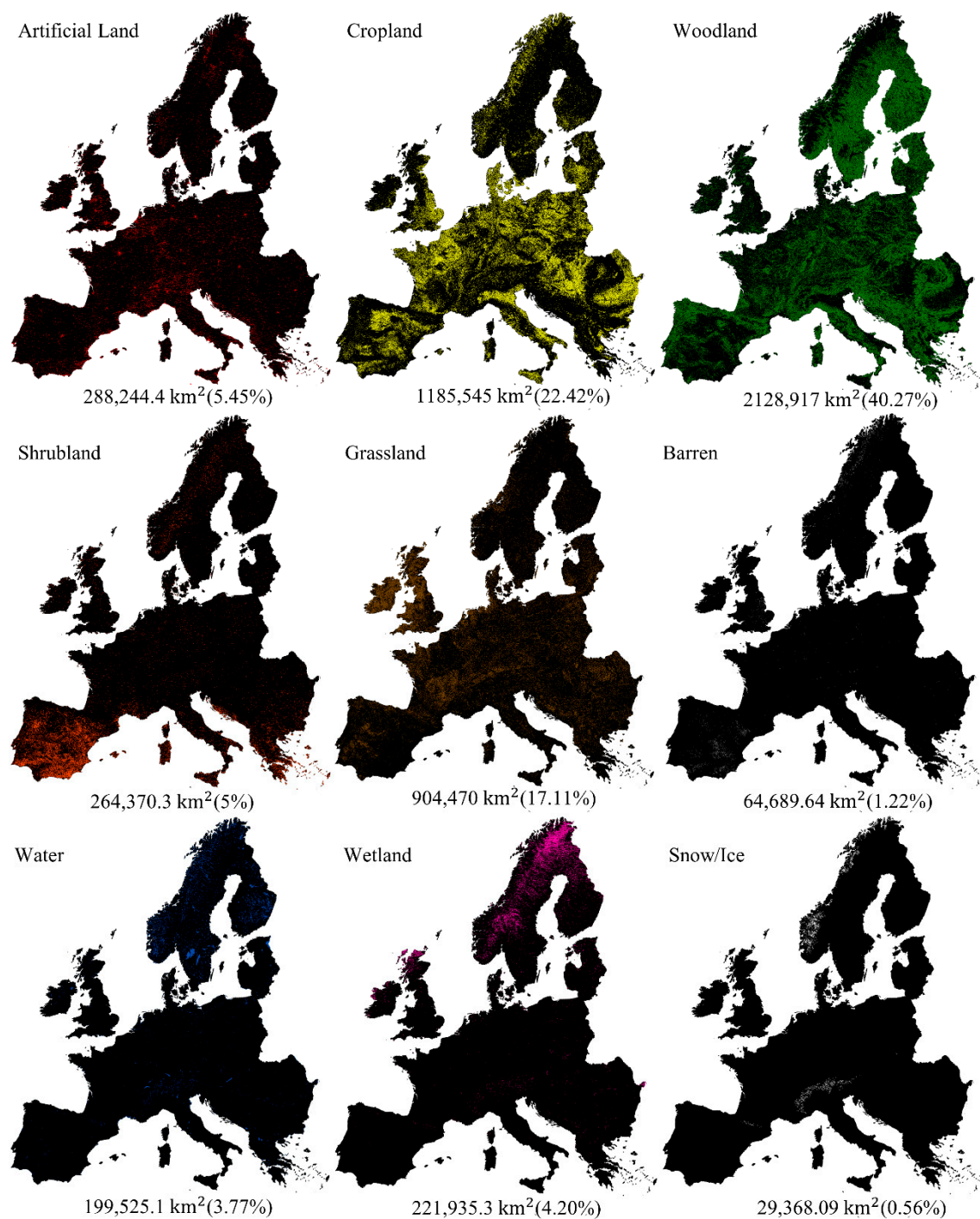


**Figure 6.** The binary maps and adjusted areas of all classes computed using [100,101] estimations, showing the extent of each class across the entire continent of Europe using the proposed methodology.

Figure 7 was also generated to supply more details of the distribution of LULC classes in seven biogeographical regions. Based on the results, Woodland is the dominant land cover across five ecozones, including Continental, Boreal, Alpine, Atlantic, and Mediterranean. Over the other two ecozones, Cropland covers more than 50% and 60% of Pannonian and Steppic, respectively. Moreover, the wet areas (i.e., Water and Wetlands classes) are mostly limited to the Alpine and Boreal regions, whereas they are rarely found in the Mediterranean region. It could be concluded that the provided results have a meaningful correlation with previous studies [18].

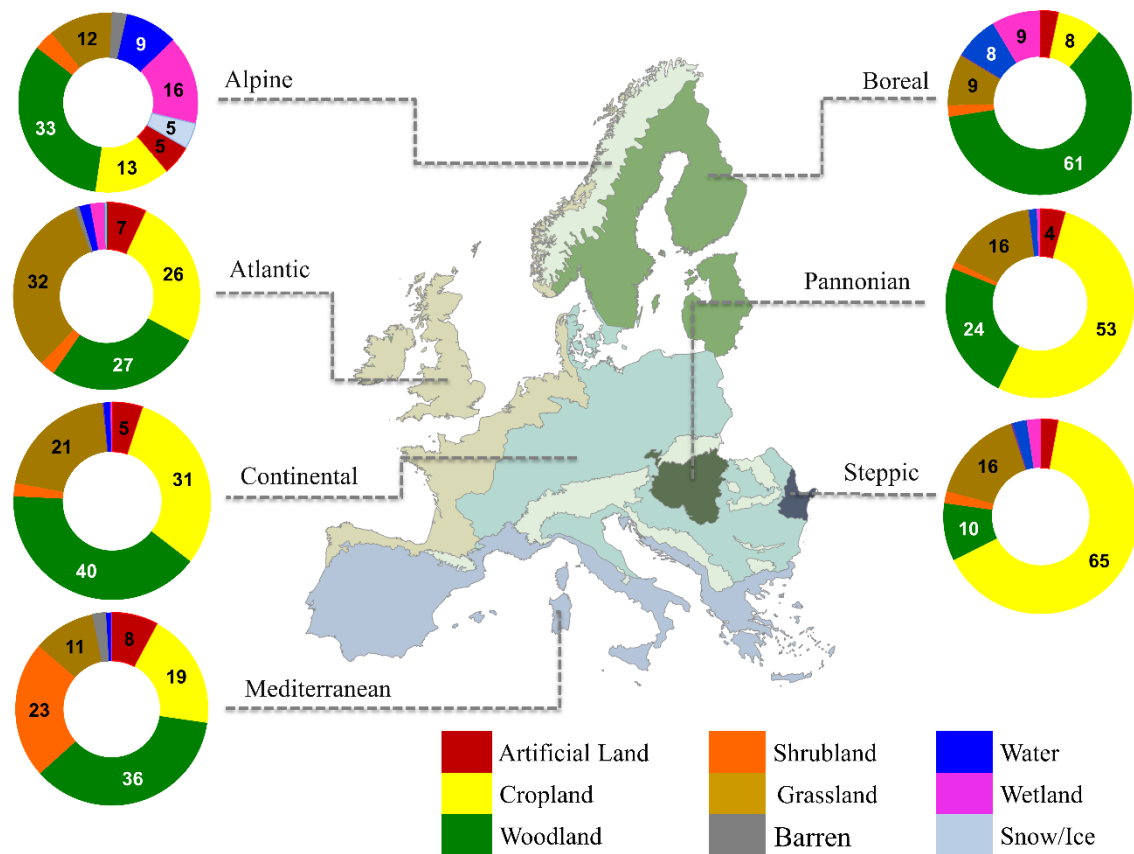


**Figure 7.** The portions of all nine LULC classes across the seven biogeographical regions.

A zoomed area of the final ELULC10-2021 was selected to visually investigate some of the classification details. It should be noted that several classes of FROM-GLC10, WorldCover 10, and S2GLC maps were reclassified to make all maps comparable (see Table A1 in Appendix A). As shown in Figure 8, our classification map can accurately distinguish between different classes over a diverse area, significantly among easily confused classes, such as Cropland and Grassland. Additionally, the proposed methodology correctly identified trivial details of the selected subset in urban areas and borders of classes, along with satisfying a determined correlation to accurate existing maps, such as WorldCover 10 and ELC-10. Furthermore, the comparison of our results with the most recent LULC maps produced in 2020 (e.g., WorldCover 10 and Esri 2020) depicts the fact that urban and natural areas have been accurately classified in ELULC-10. For a further visual interpretation, the comparison of Figure 8a to Sentinel 10 m high resolution optical (Figure 8g) and SAR (Figure 8h) images ensures the reliability of the produced map.



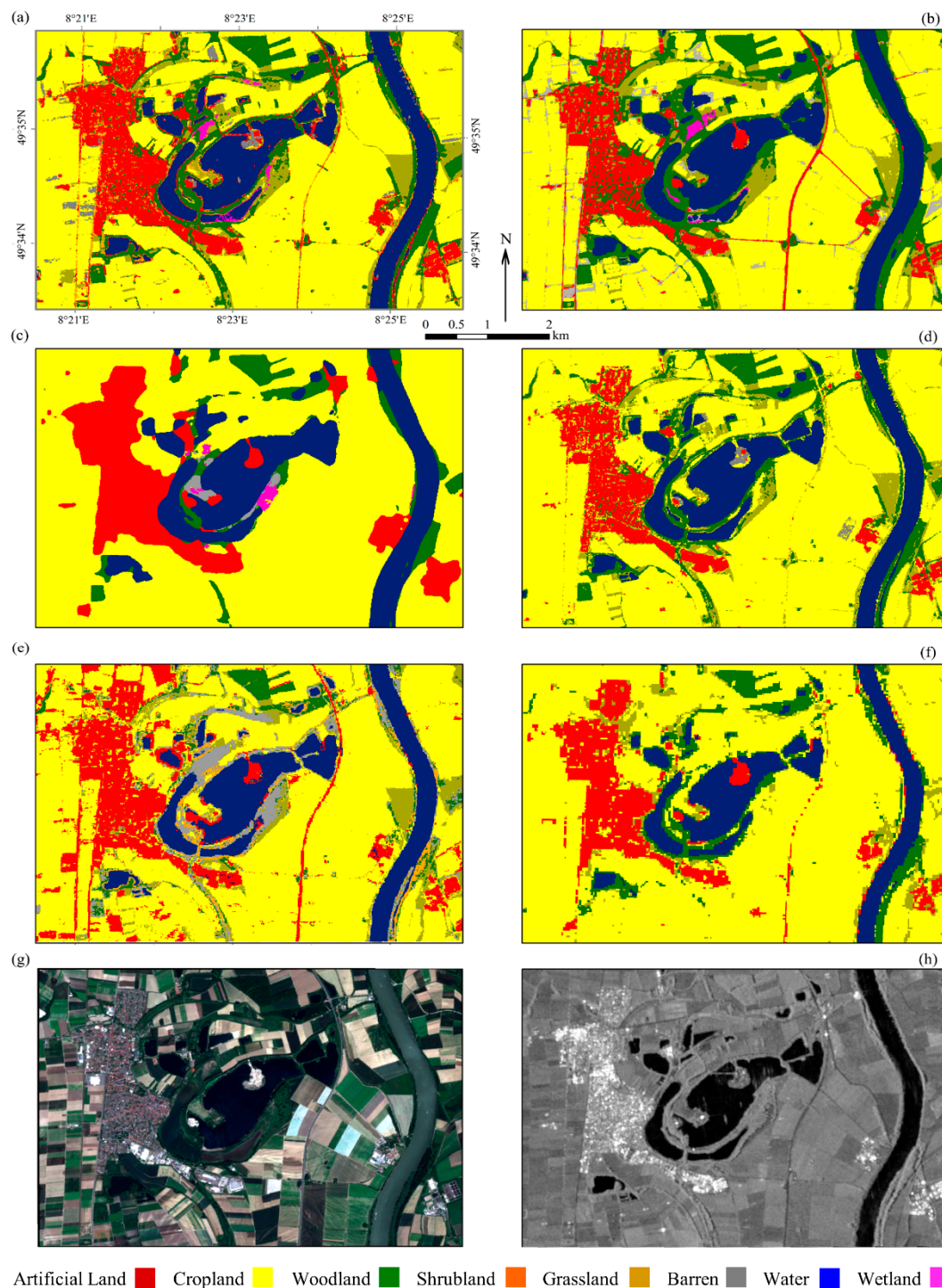


**Figure 8.** The (a) final ELULC 10 m inventory map, (b) ESA WorldCover 10 m, (c) Esri 2020, (d) ELC-10, (e) S2GLC, (f) FROM-GLC10, (g) Sentinel-2 MSI color composite images, and (h) Sentinel-1 GRD grayscale of a sample area in Silbersee, Germany.

In this study, a post-processing procedure was applied to correct misclassified covers. Figure 9 consists of the classification accuracies of ELC-10, S2GLC10, and the present study before and after post-processing. Since ELC-10 and S2GLC10 maps were only carried out on entire continent of Europe, the reported accuracies were considered for comparison purposes. In total, Figure 9 shows a 4% increase in the mapping accuracy. Although the applied rules of the post-processing procedure improved the accuracy of the Barren and Shrubland classes, their prediction was still not accurate, when compared with OA and



the accuracies of other classes. These rules also increased the classification of wetland regions by more than 5%. Figure 9 also states that the prediction of most classes was strengthened, when compared with ELC-10 and S2GLC10. The significant increase in Snow/Ice accuracy demonstrated the quality of the LUCAS dataset, since S2GLC utilized outdated CLC reference training data and only optical images. It is worth mentioning that the accuracy of ELULC-10 is also promising when compared with the national-scale map across the Europe. For instance, the most recent maps achieved 79.55%, 82%, and 90% OAs in Greece [48], Belgium [54], and Italy [53], respectively.

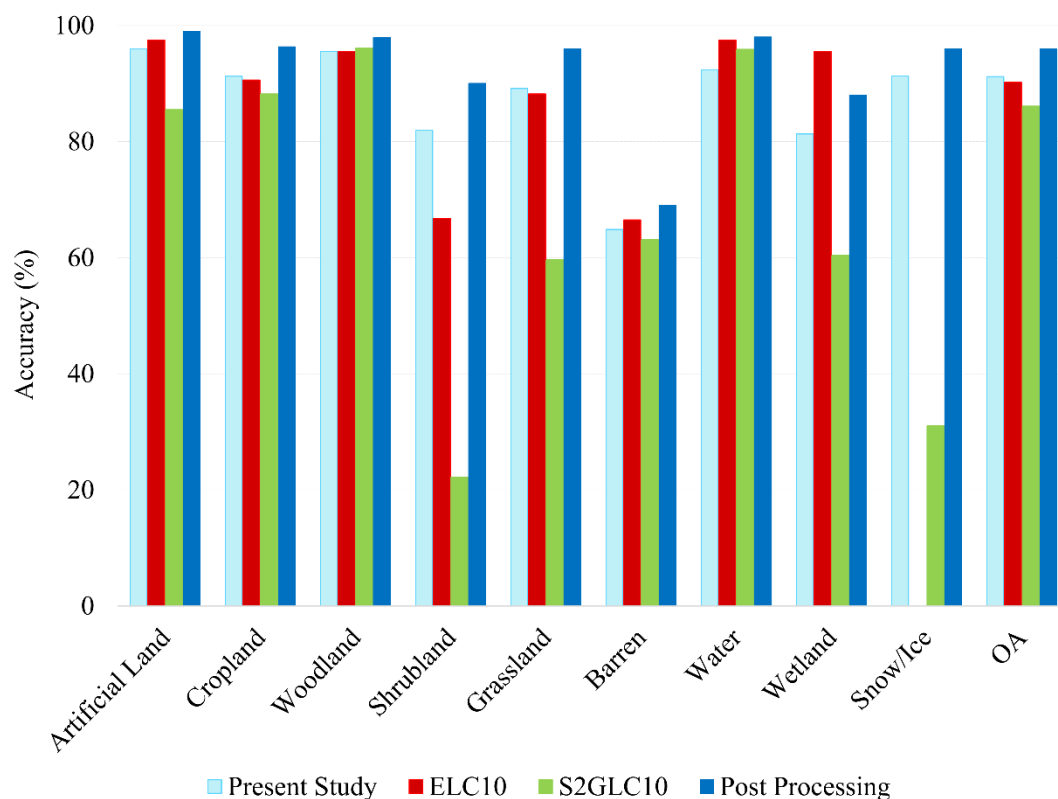


**Figure 9.** OAs and PAs of the nine LULC classes from the present study, ELC10, S2GLC10, and the present study (computed using [100,101] estimations) after post-processing.

## 5. Discussion

Despite the comparison of accuracies, several contributions were offered in the methodology of this study to enhance the quality of the final LULC map. First, the object/segment-based technique has not been proposed to generate global- or continental-scale maps. This technique can decrease the uncertainties of the pixel-based estimation [25] and create a map with minimum noise, such as salt and pepper. Moreover, a rich archive of Landsat-8, Sentinel-1 & 2 was integrated to train a classifier fulfilled by spectral (Sentinel-2 and Landsat-8) and physical (Sentinel-1) characteristics, which were not so far investigated in available global/continental maps. Landsat-8 images can also fill the gaps of Sentinel-2 data in producing NDVI time-series features. Additionally, the customized features were extracted from seasonal characteristics, which can improve the inter-class separability. Finally, a LUCAS data preparation was implemented to prepare refined reference samples from poly- and point-based datasets to decrease the uncertainties. This repository included a comparative number of samples (i.e., more than 200 K).

The LUCAS dataset offers a rich archive for LULC mapping in Europe. However, the distribution and quality of spatial sampling creates challenges for classification accuracy. For example, around 30% of LUCAS samples lack GPS precision, indicating misregistration errors of the field and image, which has already been addressed by [18,75]. Moreover,

although several sources of uncertainty were solved by d'Andrimont et al. [75], this dataset still suffers from unequal distribution and imbalances. As shown in Section 2.2.5 and Figure 1, a proper number of samples were not surveyed in several classes. For instance, a limited number of wetland samples were reported in the Alpine region, which is the most common wetland area. Additionally, there is a significant difference in the number of samples of LULC classes, such as Water, Shrubland, and Wetland. These classes cover more than 12% of European landscapes, but only 5% of LUCAS samples have been dedicated to them. It is worth mentioning that Shrubland and Wetland classes were also among the classes with the lowest accuracies in previous studies and the present work. Considering the abovementioned points, removing the obstacles in the ongoing LUCAS dataset of 2022 should enable a reliable and robust reference source, including surveying a consistent ratio of the number of samples to the extent of classes in all biogeographical regions, and performing an accurate locating service.

Thanks to ESA, USGS, and Google, a rich archive of RS data and cloud computing platforms have been provided to generate high spatial and temporal maps and address small-scale changes. Since both Sentinel-1/-2 datasets are available from 2016, the proposed methodology can provide yearly and seasonal maps, providing a piece of valuable information for natural resources studies and management. Moreover, a cross-correlation of recent LUCAS versions in 2012 and 2018 and an ongoing survey in 2022 to Sentinel images can be investigated to address the LUCAS uncertainties; this could provide a strongly correlated map of the correspondent years.

The Woodland, Cropland, and Artificial Land classes show high accuracies, emphasizing the high potential of the proposed methodology to categorize their sub-classes. Various crops, types of trees, and built areas can be classified using the sub-classes of LUCAS using the proposed methodology. For instance, spectral analysis of Sentinel-2 images integrated by Sentinel-1 time series [102,103] and dual-polarimetric ratios could significantly improve the types of trees detection and forest maps at a 10 m sampling. Frequent cropland mapping could also be performed through the proposed methodology. Considering the 6-day temporal resolution of Sentinel data, the methodology could propose frequent monitoring of the extent of monthly to yearly crops, their destruction, and intensities. It could also be implemented to frequently observe and accurately categorize croplands of more than 80 types of crops, introduced in LUCAS.

It is highly recommended to consider the present workflow for generating 10 m change maps since 2016 to report valuable changes, such as urbanization, deforestation, and crop expansion. In addition to generating temporal maps, the proposed workflow is able to supply spectral indices (e.g., NDVI and NDWI) time series, which are the most common procedure to illustrate changes by assessing positive or negative slopes of the time series. For instance, a critical deforestation caused by urbanization may be a case of study in the Woodland coverage of Boreal regions.

In addition to existing ensemble ML algorithms, GEE has recently developed its platform to apply DL algorithms. Despite the proper performance of the commonly used ML algorithms, such as RF and ANN, DL models have showed higher accuracies in LULC mapping. However, GEE infrastructure is restricted to the limited number of features and training samples, especially over large-scale areas. Therefore, rule-based post-processing was performed in this study to compensate for the shortcomings of GEE in its number of features. Furthermore, different classification algorithms have been added to the library, improving the classification robustness, including segmentation algorithms and all available ML models in Google AI Platform.

## 6. Conclusions

In addition to the freely available satellite images and ML algorithms in GEE, the computational power of this platform enables the leveraging of continental and global-scale LULC mapping. This study generated the most recent European LULC map by integrating object-based supervised learning, Sentinel-1, -2 and Landsat-8 images, and a LUCAS

reference samples dataset. A novel reference samples preparation using the ANN algorithm was also presented to remove the least accurate and noisy samples. Consequently, Europe was classified in a 10 m spatial resolution with the highest reported accuracy (OA = 91.18%). The OAs also varied from 90% to 97% across seven biogeographical regions. The proposed methodology showed that Woodland and Cropland are the most dominant LULC covers in Europe and were mapped with high accuracies (i.e., above 90%). Barren and Snow/Ice were found as the least representative classes, covering less than 2% of the study area. It was also demonstrated that Shrubland and Wetland areas are mostly isolated in the south-western and northern regions, respectively.

This study addressed two shortcomings using a novel reference sample preparation and rule-based procedure. The preparation highly improved the reliability of LUCAS datasets by integrating the original and harmonized versions and removing the noisy samples. Second, a post-processed map was generated considering the limitation of GEE in its input features. The rule-based procedures improved the quality of ELULC-10 to more than 95% OA and 0.93 KC. Overall, this study leveraged all possible European-based RS data since 2016 and LUCAS reference samples data collection, to generate an accurate European LULC map. Our mapping accuracies were almost higher than all available European and global maps. We wish to suggest that the GEE platform could improve its functionality by inputting more features and providing a separate panel for large-scale processing. Additionally, the LUCAS dataset may be fulfilled by validation efforts to restrict uncertainties and make it compatible with RS monitoring.

**Author Contributions:** Conceptualization, S.M.M. and M.A.; methodology, S.M.M., M.K., F.M., A.G. and M.A.; software, M.K., F.M. and S.M.M.; validation, F.M. and S.M.M.; data curation, S.M.M. and M.K.; writing—original draft preparation, S.M.M., M.K., F.M. and A.G.; review and editing, all authors; visualization, S.M.M., F.M. and M.K.; supervision, M.A., M.C. and O.M.; funding acquisition, M.C. All authors have read and agreed to the published version of the manuscript.

**Funding:** The APC was funded by Centre Tecnològic de Telecomunicacions de Catalunya (CTTC/CERCA), Geomatics Research Unit.

**Data Availability Statement:** Not applicable.

**Conflicts of Interest:** The authors declare no conflict of interest.

## Appendix A

**Table A1.** The reclassified classes of the available 10 m maps for the comparison assessment.

ELULC-10	ELC10	GLC10	Esri	ESA	S2GLC
Artificial land	Artificial land	Impervious	Built Area	Built-up	Artificial surfaces
Cropland	Cropland	Cropland	Crops	Cropland	- Cultivated areas - Vineyards
Woodland	Woodland	Forest	Trees	Tree cover	- Broadleaf tree cover - Coniferous tree cover
Shrubland	Shrubland	Shrubland	Scrub/shrub	Shrubland	Sclerophyllous vegetation
Grassland	Grassland	- Grassland - Tundra	Grass	Grassland	- Herbaceous vegetation - Moors and heathland
Barren	Bare land	Barren	Bare ground	- Bare/sparse vegetation - Moss and lichen	Natural material surfaces
Water	Water	Water	Water	Permanent water bodies	Water bodies

Table A1. Cont.

ELULC-10	ELC10	GLC10	Esri	ESA	S2GLC
Wetlands	Wetland	Wetland	Flooded vegetation	- Herbaceous wetland - Mangroves	- Marshes - Peatbogs
Snow/Ice	Water	Snow/ice	Snow/Ice	Snow and ice	Permanent snow cover
			Clouds		Surfaces permanently covered by cloud

## References

- Pham, H.M.; Yamaguchi, Y.; Bui, T.Q. A case study on the relation between city planning and urban growth using remote sensing and spatial metrics. *Landsc. Urban Plan.* **2011**, *100*, 223–230. [\[CrossRef\]](#)
- Coutts, A.M.; Harris, R.J.; Phan, T.; Livesley, S.J.; Williams, N.S.G.; Tapper, N.J. Thermal infrared remote sensing of urban heat: Hotspots, vegetation, and an assessment of techniques for use in urban planning. *Remote Sens. Environ.* **2016**, *186*, 637–651. [\[CrossRef\]](#)
- Wellmann, T.; Lausch, A.; Andersson, E.; Knapp, S.; Cortinovis, C.; Jache, J.; Scheuer, S.; Kremer, P.; Mascarenhas, A.; Kraemer, R.; et al. Remote sensing in urban planning: Contributions towards ecologically sound policies? *Landsc. Urban Plan.* **2020**, *204*, 103921. [\[CrossRef\]](#)
- Cavalli, R.M.; Laneve, G.; Fusilli, L.; Pignatti, S.; Santini, F. Remote sensing water observation for supporting Lake Victoria weed management. *J. Environ. Manag.* **2009**, *90*, 2199–2211. [\[CrossRef\]](#)
- Muzirafuti, A.; Boualoul, M.; Barreca, G.; Allaoui, A.; Bouikbane, H.; Lanza, S.; Crupi, A.; Randazzo, G. Fusion of remote sensing and applied geophysics for sinkholes identification in Tabular Middle Atlas of Morocco (the Causse of El Hajeb): Impact on the protection of water resource. *Resources* **2020**, *9*, 51. [\[CrossRef\]](#)
- Bock, M.; Rossner, G.; Wissen, M.; Remm, K.; Langanke, T.; Lang, S.; Klug, H.; Blaschke, T.; Vrščaj, B. Spatial indicators for nature conservation from European to local scale. *Ecol. Indic.* **2005**, *5*, 322–338. [\[CrossRef\]](#)
- Diaz-Delgado, R.; Hurford, C.; Lucas, R. Introducing the Book “The Roles of Remote Sensing in Nature Conservation.” In *The Roles of Remote Sensing in Nature Conservation*; Springer International Publishing: Berlin/Heidelberg, Germany, 2017; pp. 3–10.
- Winkler, K.; Fuchs, R.; Rounsevell, M.; Herold, M. Global land use changes are four times greater than previously estimated. *Nat. Commun.* **2021**, *12*, 2501. [\[CrossRef\]](#)
- Colwell, R.N. Remote sensing of natural resources. *Sci. Am. JSTOR* **1968**, *218*, 54–71. [\[CrossRef\]](#)
- Morales-Barquero, L.; Lyons, M.B.; Phinn, S.R.; Roelfsema, C.M. Trends in remote sensing accuracy assessment approaches in the context of natural resources. *Remote Sens.* **2019**, *11*, 2305. [\[CrossRef\]](#)
- Camalan, S.; Cui, K.; Pauca, V.P.; Alqahtani, S.; Silman, M.; Chan, R.; Plemmons, R.J.; Dethier, E.N.; Fernandez, L.E.; Lutz, D.A. Change Detection of Amazonian Alluvial Gold Mining Using Deep Learning and Sentinel-2 Imagery. *Remote Sens.* **2022**, *14*, 1746. [\[CrossRef\]](#)
- Nagendra, H. Using remote sensing to assess biodiversity. *Int. J. Remote Sens.* **2001**, *22*, 2377–2400. [\[CrossRef\]](#)
- Vogeler, J.C.; Yang, Z.; Cohen, W.B. Mapping post-fire habitat characteristics through the fusion of remote sensing tools. *Remote Sens. Environ.* **2016**, *173*, 294–303. [\[CrossRef\]](#)
- Mikula, K.; Šibíková, M.; Ambroz, M.; Kollár, M.; Ožvat, A.A.; Urbán, J.; Jarolínek, I.; Šibík, J. Naturesat—a software tool for identification, monitoring and evaluation of habitats by remote sensing techniques. *Remote Sens.* **2021**, *13*, 3381. [\[CrossRef\]](#)
- Pinter, P.J.; Hatfield, J.L.; Schepers, J.S.; Barnes, E.M.; Moran, M.S.; Daughtry, C.S.T.; Upchurch, D.R. Remote Sensing for Crop Management. *Photogramm. Eng. Remote Sens.* **2003**, *69*, 647–664. [\[CrossRef\]](#)
- Bégué, A.; Arvor, D.; Bellon, B.; Betbeder, J.; de Abelleira, D.; Ferraz, R.P.D.; Lebourgeois, V.; Lelong, C.; Simões, M.; Verón, S.R. Remote sensing and cropping practices: A review. *Remote Sens.* **2018**, *10*, 99. [\[CrossRef\]](#)
- d’Andrimont, R.; Verhegghen, A.; Lemoine, G.; Kempeneers, P.; Meroni, M.; van der Velde, M. From parcel to continental —A first European crop type map based on Sentinel-1 and LUCAS Copernicus in-situ observations. *Remote Sens. Environ.* **2021**, *266*, 112708. [\[CrossRef\]](#)
- Pflugmacher, D.; Rabe, A.; Peters, M.; Hostert, P. Mapping pan-European land cover using Landsat spectral-temporal metrics and the European LUCAS survey. *Remote Sens. Environ.* **2019**, *221*, 583–595. [\[CrossRef\]](#)
- Malinowski, R.; Lewiński, S.; Rybicki, M.; Gromny, E.; Jenerowicz, M.; Krupiński, M.; Nowakowski, A.; Wojtkowski, C.; Krupiński, M.; Krätzschmar, E.; et al. Automated production of a land cover/use map of Europe based on sentinel-2 imagery. *Remote Sens.* **2020**, *12*, 3523. [\[CrossRef\]](#)
- Gong, P.; Liu, H.; Zhang, M.; Li, C.; Wang, J.; Huang, H.; Clinton, N.; Ji, L.; Li, W.; Bai, Y.; et al. Stable classification with limited sample: Transferring a 30-m resolution sample set collected in 2015 to mapping 10-m resolution global land cover in 2017. *Sci. Bull.* **2019**, *64*, 370–373. [\[CrossRef\]](#)
- Immitzer, M.; Vuolo, F.; Atzberger, C. First experience with Sentinel-2 data for crop and tree species classifications in central Europe. *Remote Sens.* **2016**, *8*, 166. [\[CrossRef\]](#)

22. Clerici, N.; Valbuena Calderón, C.A.; Posada, J.M. Fusion of sentinel-1a and sentinel-2A data for land cover mapping: A case study in the lower Magdalena region, Colombia. *J. Maps* **2017**, *13*, 718–726. [\[CrossRef\]](#)
23. Abdi, A.M. Land cover and land use classification performance of machine learning algorithms in a boreal landscape using Sentinel-2 data. *GIScience Remote Sens.* **2020**, *57*, 1–20. [\[CrossRef\]](#)
24. Tsendbazar, N.; Herold, M.; Li, L.; Tarko, A.; de Bruin, S.; Masiliunas, D.; Lesiv, M.; Fritz, S.; Buchhorn, M.; Smets, B.; et al. Towards operational validation of annual global land cover maps. *Remote Sens. Environ.* **2021**, *266*, 112686. [\[CrossRef\]](#)
25. Venter, Z.S.; Sydenham, M.A.K. Continental-scale land cover mapping at 10 m resolution over Europe (Elc10). *Remote Sens.* **2021**, *13*, 2301. [\[CrossRef\]](#)
26. Karra, K.; Kontgis, C.; Statman-Weil, Z.; Mazzariello, J.C.; Mathis, M.; Brumby, S.P. Global land use/land cover with Sentinel 2 and deep learning. In Proceedings of the 2021 IEEE International Geoscience and Remote Sensing Symposium IGARSS, Brussels, Belgium, 11–16 July 2021; pp. 4704–4707.
27. Fuller, R.M.; Groom, G.B.; Jones, A.R. The land cover map of Great Britain: An automated classification of Landsat thematic mapper data. *Photogramm. Eng. Remote Sens.* **1994**, *60*, 553–562.
28. Hansen, M.C.; Loveland, T.R. A review of large area monitoring of land cover change using Landsat data. *Remote Sens. Environ.* **2012**, *122*, 66–74. [\[CrossRef\]](#)
29. Potapov, P.; Hansen, M.C.; Kommareddy, I.; Kommareddy, A.; Turubanova, S.; Pickens, A.; Adusei, B.; Tyukavina, A.; Ying, Q. Landsat analysis ready data for global land cover and land cover change mapping. *Remote Sens.* **2020**, *12*, 426. [\[CrossRef\]](#)
30. Gong, P.; Wang, J.; Yu, L.; Zhao, Y.; Zhao, Y.; Liang, L.; Niu, Z.; Huang, X.; Fu, H.; Liu, S.; et al. Finer resolution observation and monitoring of global land cover: First mapping results with Landsat TM and ETM+ data. *Int. J. Remote Sens.* **2013**, *34*, 2607–2654. [\[CrossRef\]](#)
31. Andres, L.; Salas, W.A.; Skole, D. Fourier analysis of multi-temporal AVHRR data applied to a land cover classification. *Int. J. Remote Sens.* **1994**, *15*, 1115–1121. [\[CrossRef\]](#)
32. Ali, S.; Henchiri, M.; Sha, Z.; Wilson, K.; Yun, B.; Yao, F.; Zhang, J. A time series of land cover maps of South Asia from 2001 to 2015 generated using AVHRR GIMMS NDVI3g data. *Environ. Sci. Pollut. Res.* **2020**, *27*, 20309–20320. [\[CrossRef\]](#)
33. Thenkabail, P.S.; Gangadhara Rao, P.; Biggs, T.W.; Krishna, M.; Tural, H. Spectral matching techniques to determine historical Land-use/Land-cover (LULC) and irrigated areas using time-series 0.1-degree AVHRR pathfinder datasets. *Photogramm. Eng. Remote Sens.* **2007**, *73*, 1029–1040.
34. Strahler, A.; Muchoney, D.; Jordan, B.; Friedl, M.; Gopal, S.; Lambin, E.; Moody, A. MODIS Land Cover Product Algorithm Theoretical Basis Document (ATBD) MODIS Land Cover and Land-Cover Change. *MODIS Doc.* **1999**, *42*, 47.
35. Friedl, M.A.; McIver, D.K.; Hodges, J.C.F.; Zhang, X.Y.; Muchoney, D.; Strahler, A.H.; Woodcock, C.E.; Gopal, S.; Schneider, A.; Cooper, A.; et al. Global land cover mapping from MODIS: Algorithms and early results. *Remote Sens. Environ.* **2002**, *83*, 287–302. [\[CrossRef\]](#)
36. Sulla-Menashe, D.; Gray, J.M.; Abercrombie, S.P.; Friedl, M.A. Hierarchical mapping of annual global land cover 2001 to present: The MODIS Collection 6 Land Cover product. *Remote Sens. Environ.* **2019**, *222*, 183–194. [\[CrossRef\]](#)
37. Amani, M.; Brisco, B.; Afshar, M.; Mirmazloumi, S.M.; Mahdavi, S.; Mirzadeh, S.M.J.; Huang, W.; Granger, J. A generalized supervised classification scheme to produce provincial wetland inventory maps: An application of Google Earth Engine for big geo data processing. *Big Earth Data* **2019**, *3*, 378–394. [\[CrossRef\]](#)
38. Gorelick, N.; Hancher, M.; Dixon, M.; Ilyushchenko, S.; Thau, D.; Moore, R. Google Earth Engine: Planetary-scale geospatial analysis for everyone. *Remote Sens. Environ.* **2017**, *202*, 18–27. [\[CrossRef\]](#)
39. Amani, M.; Ghorbanian, A.; Ahmadi, S.A.; Kakooei, M.; Moghimi, A.; Mirmazloumi, S.M.; Moghaddam, S.H.A.; Mahdavi, S.; Ghahremanloo, M.; Parsian, S.; et al. Google Earth Engine Cloud Computing Platform for Remote Sensing Big Data Applications: A Comprehensive Review. *IEEE J. Sel. Top. Appl. Earth Obs. Remote Sens.* **2020**, *13*, 5326–5350. [\[CrossRef\]](#)
40. Kumar, L.; Mutanga, O. Google Earth Engine applications since inception: Usage, trends, and potential. *Remote Sens.* **2018**, *10*, 1509. [\[CrossRef\]](#)
41. Tamiminia, H.; Salehi, B.; Mahdianpari, M.; Quackenbush, L.; Adeli, S.; Brisco, B. Google Earth Engine for geo-big data applications: A meta-analysis and systematic review. *ISPRS J. Photogramm. Remote Sens.* **2020**, *164*, 152–170. [\[CrossRef\]](#)
42. Li, Q.; Qiu, C.; Ma, L.; Schmitt, M.; Zhu, X.X. Mapping the land cover of Africa at 10 m resolution from multi-source remote sensing data with Google Earth Engine. *Remote Sens.* **2020**, *12*, 602. [\[CrossRef\]](#)
43. Ghorbanian, A.; Kakooei, M.; Amani, M.; Mahdavi, S.; Mohammadzadeh, A.; Hasanlou, M. Improved land cover map of Iran using Sentinel imagery within Google Earth Engine and a novel automatic workflow for land cover classification using migrated training samples. *ISPRS J. Photogramm. Remote Sens.* **2020**, *167*, 276–288. [\[CrossRef\]](#)
44. Land-cover maps of Europe from the Cloud. Available online: [https://www.esa.int/Applications/Observing\\_the\\_Earth/Copernicus/Sentinel-2/Land-cover\\_maps\\_of\\_Europe\\_from\\_the\\_Cloud#.YLIADWazCxU.link](https://www.esa.int/Applications/Observing_the_Earth/Copernicus/Sentinel-2/Land-cover_maps_of_Europe_from_the_Cloud#.YLIADWazCxU.link) (accessed on 30 May 2022).
45. In Proceedings of the ESA 2017 WorldCover Conference, Frascati, Italy, 14–16 March 2017. Available online: <http://worldcover2017.esa.int/> (accessed on 30 May 2022).
46. Zanaga, D.; Van De Kerchove, R.; De Keersmaecker, W.; Souverijns, N.; Brockmann, C.; Quast, R.; Wevers, J.; Grosu, A.; Paccini, A.; Vergnaud, S.; et al. ESA WorldCover 10 m 2020 v100. Zenodo. 2021. Available online: <https://zenodo.org/record/5571936#.YrV38HZByUK> (accessed on 30 May 2022).



47. Buchhorn, M.; Bertels, L.; Smets, B.; De Roo, B.; Lesiv, M.; Tsendbazar, N.E.; Masiliunas, D.; Li, L. *Copernicus Global Land Service: Land Cover 100m: Version 3 Globe 2015–2019: Algorithm Theoretical Basis Document*; ESA: Paris, France, 2020.
48. Verde, N.; Kokkoris, I.P.; Georgiadis, C.; Kaimaris, D.; Dimopoulos, P.; Mitsopoulos, I.; Mallinis, G. National scale land cover classification for ecosystem services mapping and assessment, using multitemporal copernicus EO data and google earth engine. *Remote Sens.* **2020**, *12*, 3303. [\[CrossRef\]](#)
49. Gounaridis, D.; Apostolou, A.; Koukoulas, S. Land cover of Greece, 2010: A semi-automated classification using random forests. *J. Maps* **2016**, *12*, 1055–1062. [\[CrossRef\]](#)
50. Inglada, J.; Vincent, A.; Arias, M.; Tardy, B.; Morin, D.; Rodes, I. Operational High Resolution Land Cover Map Production at the Country Scale Using Satellite Image Time Series. *Remote Sens.* **2017**, *9*, 95. [\[CrossRef\]](#)
51. Mack, B.; Leinenkugel, P.; Kuenzer, C.; Dech, S. A semi-automated approach for the generation of a new land use and land cover product for Germany based on Landsat time-series and Lucas in-situ data. *Remote Sens. Lett.* **2017**, *8*, 244–253. [\[CrossRef\]](#)
52. Congedo, L.; Sallustio, L.; Munafò, M.; Ottaviano, M.; Tonti, D.; Marchetti, M. Copernicus high-resolution layers for land cover classification in Italy. *J. Maps* **2016**, *12*, 1195–1205. [\[CrossRef\]](#)
53. De Fioravante, P.; Strollo, A.; Assennato, F.; Marinosci, I.; Congedo, L.; Munafò, M. High resolution land cover integrating copernicus products: A 2012–2020 map of Italy. *Land* **2022**, *11*, 35. [\[CrossRef\]](#)
54. Van Tricht, K.; Gobin, A.; Gilliams, S.; Piccard, I. Synergistic use of radar sentinel-1 and optical sentinel-2 imagery for crop mapping: A case study for Belgium. *Remote Sens.* **2018**, *10*, 1642. [\[CrossRef\]](#)
55. Fritz, S.; See, L.; McCallum, I.; You, L.; Bun, A.; Moltchanova, E.; Duerauer, M.; Albrecht, F.; Schill, C.; Perger, C.; et al. Mapping global cropland and field size. *Glob. Chang. Biol.* **2015**, *21*, 1980–1992. [\[CrossRef\]](#)
56. Cao, X.; Chen, X.H.; Zhang, W.W.; Liao, A.P.; Chen, L.J.; Chen, Z.G.; Chen, J. Global cultivated land mapping at 30 m spatial resolution. *Sci. China Earth Sci.* **2016**, *59*, 2275–2284. [\[CrossRef\]](#)
57. Chen, J.; Chen, J.; Liao, A.; Cao, X.; Chen, L.; Chen, X.; He, C.; Han, G.; Peng, S.; Lu, M.; et al. Global land cover mapping at 30 m resolution: A POK-based operational approach. *ISPRS J. Photogramm. Remote Sens.* **2015**, *103*, 7–27. [\[CrossRef\]](#)
58. Qu, L.; Chen, Z.; Li, M.; Zhi, J.; Wang, H. Accuracy improvements to pixel-based and object-based LULC classification with auxiliary datasets from google earth engine. *Remote Sens.* **2021**, *13*, 453. [\[CrossRef\]](#)
59. Feizizadeh, B.; Omarzadeh, D.; Kazemi Garajeh, M.; Lakes, T.; Blaschke, T. Machine learning data-driven approaches for land use/cover mapping and trend analysis using Google Earth Engine. *J. Environ. Plan. Manag.* **2021**. [\[CrossRef\]](#)
60. Stromann, O.; Nascetti, A.; Yousif, O.; Ban, Y. Dimensionality Reduction and Feature Selection for Object-Based Land Cover Classification based on Sentinel-1 and Sentinel-2 Time Series Using Google Earth Engine. *Remote Sens.* **2020**, *12*, 76. [\[CrossRef\]](#)
61. Tassi, A.; Vizzari, M. Object-oriented lulc classification in google earth engine combining snic, glcm, and machine learning algorithms. *Remote Sens.* **2020**, *12*, 3776. [\[CrossRef\]](#)
62. Shafizadeh-Moghadam, H.; Khazaei, M.; Alavipanah, S.K.; Weng, Q. Google Earth Engine for large-scale land use and land cover mapping: An object-based classification approach using spectral, textural and topographical factors. *GIScience Remote Sens.* **2021**, *58*, 914–928. [\[CrossRef\]](#)
63. EEA Land cover country fact sheets 2000–2018. Available online: [https://www.eea.europa.eu/ds\\_resolveuid/03ba369bb3064fd1a77c8361ab4b0eed](https://www.eea.europa.eu/ds_resolveuid/03ba369bb3064fd1a77c8361ab4b0eed) (accessed on 30 May 2022).
64. Google Earth Engine Sentinel-1 Algorithms. Available online: <https://developers.google.com/earth-engine/guides/sentinel1> (accessed on 30 May 2022).
65. Abrams, M.; Crippen, R.; Fujisada, H. ASTER Global Digital Elevation Model (GDEM) and ASTER Global Water Body Dataset (ASTWBD). *Remote Sens.* **2020**, *12*, 1156. [\[CrossRef\]](#)
66. Nikolakopoulos, K.G.; Kamaratakis, E.K.; Chrysoulakis, N. SRTM vs ASTER elevation products. Comparison for two regions in Crete, Greece. *Int. J. Remote Sens.* **2006**, *27*, 4819–4838. [\[CrossRef\]](#)
67. Gallego, J. Fine scale profile of CORINE Land Cover classes with LUCAS data. In *Building Agri-Environmental Indicators: Focussing on the European Area Frame Survey LUCAS*; Institute for Environment and Sustainability JRC: Ispra, Italy, 2002; pp. 121–136. ISBN 92-894-4633-1.
68. Büttner, G.; Maucha, G. *The Thematic Accuracy of Corine Land Cover 2000. Assessment Using LUCAS (Land Use/Cover Area Frame Statistical Survey)*; European Environmental Agency: Copenhagen, Denmark, 2006.
69. Gallego, J.; Bamps, C. Using CORINE land cover and the point survey LUCAS for area estimation. *Int. J. Appl. Earth Obs. Geoinf.* **2008**, *10*, 467–475. [\[CrossRef\]](#)
70. Gallego, F.J. Validation of GIS layers in the EU: Getting adapted to available reference data. *Int. J. Digit. Earth* **2011**, *4*, 42–57. [\[CrossRef\]](#)
71. Karydas, C.G.; Gitas, I.Z.; Kuntz, S.; Minakou, C. Use of LUCAS LC point database for validating country-scale land cover maps. *Remote Sens.* **2015**, *7*, 5012–5041. [\[CrossRef\]](#)
72. Esch, T.; Metz, A.; Marconcini, M.; Keil, M. Combined use of multi-seasonal high and medium resolution satellite imagery for parcel-related mapping of cropland and grassland. *Int. J. Appl. Earth Obs. Geoinf.* **2014**, *28*, 230–237. [\[CrossRef\]](#)
73. Leinenkugel, P.; Deck, R.; Huth, J.; Ottinger, M.; Mack, B. The potential of open geodata for automated large-scale land use and land cover classification. *Remote Sens.* **2019**, *11*, 2249. [\[CrossRef\]](#)
74. E4.LUCAS (ESTAT). LUCAS 2018 (Land Use/Cover Area Frame Survey). 2018. Available online: <https://ec.europa.eu/eurostat/web/lucas/data/primary-data/2018> (accessed on 30 May 2022).

75. d'Andrimont, R.; Yordanov, M.; Martinez-Sanchez, L.; Eiselt, B.; Palmieri, A.; Dominici, P.; Gallego, J.; Reuter, H.I.; Joebges, C.; Lemoine, G.; et al. Harmonised LUCAS in-situ land cover and use database for field surveys from 2006 to 2018 in the European Union. *Sci. Data* **2020**, *7*, 352. [\[CrossRef\]](#)
76. Ghorbanian, A.; Zaghian, S.; Asiyabi, R.M.; Amani, M.; Mohammadzadeh, A.; Jamali, S. Mangrove ecosystem mapping using sentinel-1 and sentinel-2 satellite images and random forest algorithm in google earth engine. *Remote Sens.* **2021**, *13*, 2565. [\[CrossRef\]](#)
77. Li, H.; Zhang, C.; Zhang, S.; Atkinson, P.M. Crop classification from full-year fully-polarimetric L-band UAVSAR time-series using the Random Forest algorithm. *Int. J. Appl. Earth Obs. Geoinf.* **2020**, *87*, 102032. [\[CrossRef\]](#)
78. Hu, Y.; Tian, B.; Yuan, L.; Li, X.; Huang, Y.; Shi, R.; Jiang, X.; Wang, L.; Sun, C. Mapping coastal salt marshes in China using time series of Sentinel-1 SAR. *ISPRS J. Photogramm. Remote Sens.* **2021**, *173*, 122–134. [\[CrossRef\]](#)
79. Main-Knorn, M.; Pflug, B.; Louis, J.; Debaecker, V.; Müller-Wilm, U.; Gascon, F. Sen2Cor for Sentinel-2. In Proceedings of the Image and Signal Processing for Remote Sensing XXIII, Warsaw, Poland, 11–13 September 2017; p. 3.
80. Amani, M.; Mahdavi, S.; Afshar, M.; Brisco, B.; Huang, W.; Mirzadeh, S.M.J.; White, L.; Banks, S.; Montgomery, J.; Hopkinson, C. Canadian wetland inventory using Google Earth Engine: The first map and preliminary results. *Remote Sens.* **2019**, *11*, 842. [\[CrossRef\]](#)
81. Vermote, E.; Roger, J.C.; Franch, B.; Skakun, S. LASRC (Land Surface Reflectance Code): Overview, application and validation using MODIS, VIIRS, LANDSAT and Sentinel 2 data's. In Proceedings of the International Geoscience and Remote Sensing Symposium (IGARSS), Valencia, Spain, 22–27 July 2018; Volume 2018, pp. 8173–8176.
82. Vermote, E.; Justice, C.; Claverie, M.; Franch, B. Preliminary analysis of the performance of the Landsat 8/OLI land surface reflectance product. *Remote Sens. Environ.* **2016**, *185*, 46–56. [\[CrossRef\]](#)
83. Mohammadi Asiyabi, R.; Sahebi, M.R.; Ghorbanian, A. Segment-based bag of visual words model for urban land cover mapping using polarimetric SAR data. *Adv. Space Res.* **2021**, *in press*. [\[CrossRef\]](#)
84. Ai, J.; Zhang, C.; Chen, L.; Li, D. Mapping annual land use and land cover changes in the Yangtze Estuary Region using an object-based classification framework and landsat time series data. *Sustainability* **2020**, *12*, 659. [\[CrossRef\]](#)
85. Belgii, M.; Csillik, O. Sentinel-2 cropland mapping using pixel-based and object-based time-weighted dynamic time warping analysis. *Remote Sens. Environ.* **2018**, *204*, 509–523. [\[CrossRef\]](#)
86. Amani, M.; Mahdavi, S.; Kakooei, M.; Ghorbanian, A.; Brisco, B.; Delancey, E.; Toure, S.; Reyes, E.L. Wetland Change Analysis in Alberta, Canada Using Four Decades of Landsat Imagery. *IEEE J. Sel. Top. Appl. Earth Obs. Remote Sens.* **2021**, *14*, 10314–10335. [\[CrossRef\]](#)
87. Mahdavi, S.; Salehi, B.; Amani, M.; Granger, J.E.; Brisco, B.; Huang, W.; Hanson, A. Object-Based Classification of Wetlands in Newfoundland and Labrador Using Multi-Temporal PolSAR Data. *Can. J. Remote Sens.* **2017**, *43*, 432–450. [\[CrossRef\]](#)
88. Achanta, R.; Süsstrunk, S. Superpixels and polygons using simple non-iterative clustering. In Proceedings of the 30th IEEE Conference on Computer Vision and Pattern Recognition, CVPR 2017, Honolulu, HI, USA, 21–26 July 2017; Volume 2017, pp. 4895–4904.
89. Google Earth Engine SNIC (Simple Non-Iterative Clustering). Available online: <https://developers.google.com/earth-engine/apidocs/ee-algorithms-image-segmentation-snic> (accessed on 30 May 2022).
90. Kakooei, M.; Mining, Y.B.-J. VHR Semantic Labeling by Random Forest Classification and Fusion of Spectral and Spatial Features on Google Earth Engine. *J. AI Data Min.* **2020**, *8*, 357–370. [\[CrossRef\]](#)
91. Wang, X.; Xu, M.; Xiong, X.; Ning, C. Remote Sensing Scene Classification Using Heterogeneous Feature Extraction and Multi-Level Fusion. *IEEE Access* **2020**, *8*, 217628–217641. [\[CrossRef\]](#)
92. Amani, M.; Kakooei, M.; Moghimi, A.; Ghorbanian, A.; Ranjgar, B.; Mahdavi, S.; Davidson, A.; Fisette, T.; Rollin, P.; Brisco, B.; et al. Application of google earth engine cloud computing platform, sentinel imagery, and neural networks for crop mapping in Canada. *Remote Sens.* **2020**, *12*, 3561. [\[CrossRef\]](#)
93. Ahooei Nezhad, S.S.; Valadan Zoej, M.J.; Ghorbanian, A. A fast non-iterative method for the object to image space best scanline determination of spaceborne linear array pushbroom images. *Adv. Space Res.* **2021**, *68*, 3584–3593. [\[CrossRef\]](#)
94. Sun, C.; Bian, Y.; Zhou, T.; Pan, J. Using of multi-source and multi-temporal remote sensing data improves crop-type mapping in the subtropical agriculture region. *Sensors* **2019**, *19*, 2401. [\[CrossRef\]](#)
95. Jamali, A. Improving land use land cover mapping of a neural network with three optimizers of multi-verse optimizer, genetic algorithm, and derivative-free function. *Egypt. J. Remote Sens. Sp. Sci.* **2021**, *24*, 373–390. [\[CrossRef\]](#)
96. Chermprayong, P.; Hongkarnjanakul, N.; Rouquette, D.; Schwob, C.; Mezeix, L. Convolutional Neural Network for Thailand's Eastern Economic Corridor (EEC) land cover classification using overlapping process on satellite images. *Remote Sens. Appl. Soc. Environ.* **2021**, *23*, 100543. [\[CrossRef\]](#)
97. Erinjery, J.J.; Singh, M.; Kent, R. Mapping and assessment of vegetation types in the tropical rainforests of the Western Ghats using multispectral Sentinel-2 and SAR Sentinel-1 satellite imagery. *Remote Sens. Environ.* **2018**, *216*, 345–354. [\[CrossRef\]](#)
98. Emparanza, P.R.; Hongkarnjanakul, N.; Rouquette, D.; Schwob, C.; Mezeix, L. Land cover classification in Thailand's Eastern Economic Corridor (EEC) using convolutional neural network on satellite images. *Remote Sens. Appl. Soc. Environ.* **2020**, *20*, 100394. [\[CrossRef\]](#)
99. Kingma, D.P.; Ba, J.L. Adam: A method for stochastic optimization. In Proceedings of the 3rd International Conference on Learning Representations, ICLR 2015—Conference Track Proceedings, San Diego, CA, USA, 7–9 May 2015.

100. Olofsson, P.; Foody, G.M.; Stehman, S.V.; Woodcock, C.E. Making better use of accuracy data in land change studies: Estimating accuracy and area and quantifying uncertainty using stratified estimation. *Remote Sens. Environ.* **2013**, *129*, 122–131. [[CrossRef](#)]
101. Olofsson, P.; Foody, G.M.; Herold, M.; Stehman, S.V.; Woodcock, C.E.; Wulder, M.A. Good practices for estimating area and assessing accuracy of land change. *Remote Sens. Environ.* **2014**, *148*, 42–57. [[CrossRef](#)]
102. Liu, Y.; Gong, W.; Hu, X.; Gong, J. Forest type identification with random forest using Sentinel-1A, Sentinel-2A, multi-temporal Landsat-8 and DEM data. *Remote Sens.* **2018**, *10*, 946. [[CrossRef](#)]
103. Waser, L.T.; Rüetschi, M.; Psomas, A.; Small, D.; Rehus, N. Mapping dominant leaf type based on combined Sentinel-1/-2 data—Challenges for mountainous countries. *ISPRS J. Photogramm. Remote Sens.* **2021**, *180*, 209–226. [[CrossRef](#)]